ERDC/CRREL TR-03-XX

Cold Regions Research and Engineering Laboratory

PAVEMENT SUBGRADE PERFORMANCE STUDY

US Army Corps of Engineers®
Engineer Research and Development Center

Test Section 705

Subgrade soil type A-4 at extreme wet of optimum

Draft

Edel R. Cortez and Vincent C. Janoo

February 2003

Subgrade Moisture Content	AASHTO Soil Type			
	A-2-4	A-4	A-6	A-7-6
M1	Optimum 10 % TS 701	Optimum 17 % TS 702	Optimum 16 %	Optimum TBD*
M2	15 % TS 703	19 % TS 704	22 % TS 706	TBD
M3	12 % TS 707	23 % TS 705	19 % TS 708	TBD

CONTENTS

ILLUSTRATIONS

TABLES

EXECUTIVE SUMMARY

This is one of a series of reports on the subgrade performance research study. The hypothesis for this study is that the failure criterion depends on the subgrade type and the in-situ moisture content. Many of the current mechanistic design procedures incorporate the results from AASHO Road Tests conducted in the late fifties. However, the AASHO Road Tests were all conducted on only one soil type (AASHTO type A-6). The tests results reflect the combined effect of traffic loads and seasonal variations. Applying failure criteria based on the AASHO Road Tests to other soil types, at different moisture contents and different climate creates much uncertainty.

In recent decades much progress has been achieved in computer technology and new sensors allow reliable in-situ stress and strain measurements. The authors recognize the technological opportunities to develop more reliable pavement failure criteria that consider the effects of subgrade soil type and moisture condition.

Transportations agencies from several US states are contributing to a research initiative that will develop the bases for new pavement failure criteria that is adequate for the most common subgrade soil types found in the United State at various soil moisture contents. As part of the research program, four subgrade soils were selected for testing in the Frost Effects Research Facility (FERF). Each subgrade soil was to be constructed at three moisture contents, with one at or near optimum density and moisture content. The test sections, consisting of 75 mm of asphalt concrete and 229 mm of crushed base over the test subgrade soil, were instrumented with stress, strain, moisture, and temperature sensors. The test sections were then subjected to accelerated loading under controlled environmental conditions.

This report presents the results from the accelerated pavement for one of the test subgrade soil. According to the AASHTO soil classification system, the subgrade soil was type A-4. According to the Unified Soil Classification System, the subgrade soil was type CL (low liquid limit clay). The moisture content for this experiment was designed to be as wet as it could be constructed. The subgrade moisture content, as measured during construction, was about 23 percent. Accelerated pavement tests were conducted on five test windows in the test section. Each test window was approximately 6.0 m long and 1 m wide. Loading was applied unidirectionally at an average speed of 12 km/hr. The test section, barring any breakdowns, was subjected to about 600 load repetitions per hour. Testing was conducted for 22 hours per day. The remaining 2 hours were used for maintenance. The load was varied for each test window, ranging from 17.8 (4,012 lb) to 53.7 kN (12,081 lb). The load was applied through dual truck tires, with the tire pressures averaging 689 kPa (100 psi).

Stress, strain, and surface rut measurements were taken periodically. Stress measurements were recorded in five of the six windows. The remaining test window was damaged by the weight of the Heavy Vehicle Simulator (HVS) supports during the testing of neighboring test windows. Geokon® stress sensors were embedded in the middle of the depth of the base course at two test windows. Dynatest® stress sensors were embedded in a tri-axial arrangement in the subgrade at a depth of 0.076 m (3 in) from the top of the

subgrade in all the test windows. Two of the test windows contained an additional tri-axial set of Dynatest stress cells at a depth of 0.23 m (9 in) from the top of the subgrade.

Dynamic and permanent strains in the base and subgrade were measured in each of the five test windows.

This report presents the measured response of the pavement test section to accelerated loading. It was found that for this AASHTO A-4 soil at 23 percent moisture content, the subgrade bearing capacity was very low. Even a small number of traffic passes caused very large surface and subsurface deformations. Building a pavement structure on such soft soil was a significant challenge. Construction traffic caused large deformations observed on the top of the base course. This resulted in irregular asphalt pavement thickness that may have affected the test results. Also, the properties of the asphalt concrete were somewhat modified by a spill of hydraulic oil that resulted from a mechanical failure of the HVS. The effect of the hydraulic oil spill was primarily manifested in test window c4. Surface rutting on this test window grew rapidly beyond failure in less than 50 traffic passes despite a relatively low load. Embedded sensors measured very large permanent strains and very little stresses. A forensic evaluation was conducted at the end of traffic tests. Forensic evidence indicates that significant consolidation occurred in the subgrade soil. The shape of the surface profiles suggests that more deformation occurred at acceleration end of the test window than the opposite end. This suggests significant visco-plastic behavior. Clearly, failure criteria derived from the AASHO Road Tests are not adequate for this pavement. Additional results from other test sections will be used to validate the findings from these tests.

1 INTRODUCTION

Test Section 705 is one of twelve test sections that are currently included in a pooled-fund study on pavement subgrade performance headed by the Federal Highway Administration with the participation of 19 US states. The test sections are constructed in the Frost Effects Research Facility of the US Army Cold Regions Research and Engineering Laboratory, a component of the US Army Corps of Engineers Research and Engineering Center.

Table 1. Subgrade soil types and moisture contents included in this study.

Subgrade Moisture Content	AASHTO Soil Type			
	A-2-4	A-4	A-6	A-7-6
M1	Optimum 10 % TS 701	Optimum 17 % TS 702	Optimum 16 %	Optimum TBD*
M2	15 % TS 703	19 % TS 704	22 % TS 706	TBD
M3	12 % TS 707	23 % TS 705	19 % TS 708	TBD

* TBD = To be devised.

This reports deals with the construction, accelerated traffic testing, and pavement response of Test Section 705. Test Section 705 corresponds to a subgrade soil AASHTO type A-4 conditioned at 23 percent moisture content. At this moisture content, the subgrade soil was very soft. It was difficult to build because it deformed easily under construction traffic. This resulted in significant thickness variations in the asphalt concrete.

2 DESCRIPTION OF THE TEST SECTION

The test section consists of a 76-mm (3 in) asphalt concrete (AC) layer, a 229-mm (9 in) crushed gravel base course, and 3 m of AASHTO A-6 subgrade soil conditioned to a gravimetric moisture content of 23 percent.

The test section was divided into six test windows. A test window is the area where traffic is applied. An effective test window was 0.91 m (3 ft) wide by 6.08 m (20 ft.) long, excluding acceleration and deceleration areas. The thickness and material properties for all test windows were intended to be constant, but the traffic load was designed to vary for different test windows.

Each test window was instrumented with embedded sensors to measure in-situ stress, strain, moisture and temperature at various locations within the pavement structure. Dynatest® stress cells were used to measure stress in the subgrade soil. Geokon® stress cells were embedded in the unbound base course. Strain was deducted from displacement measurements obtained by means of emu coil pairs. Vitel Hydra® sensors were used to record volumetric soil moisture content and temperature. Additionally, strings of thermocouples were used to record subgrade temperatures.

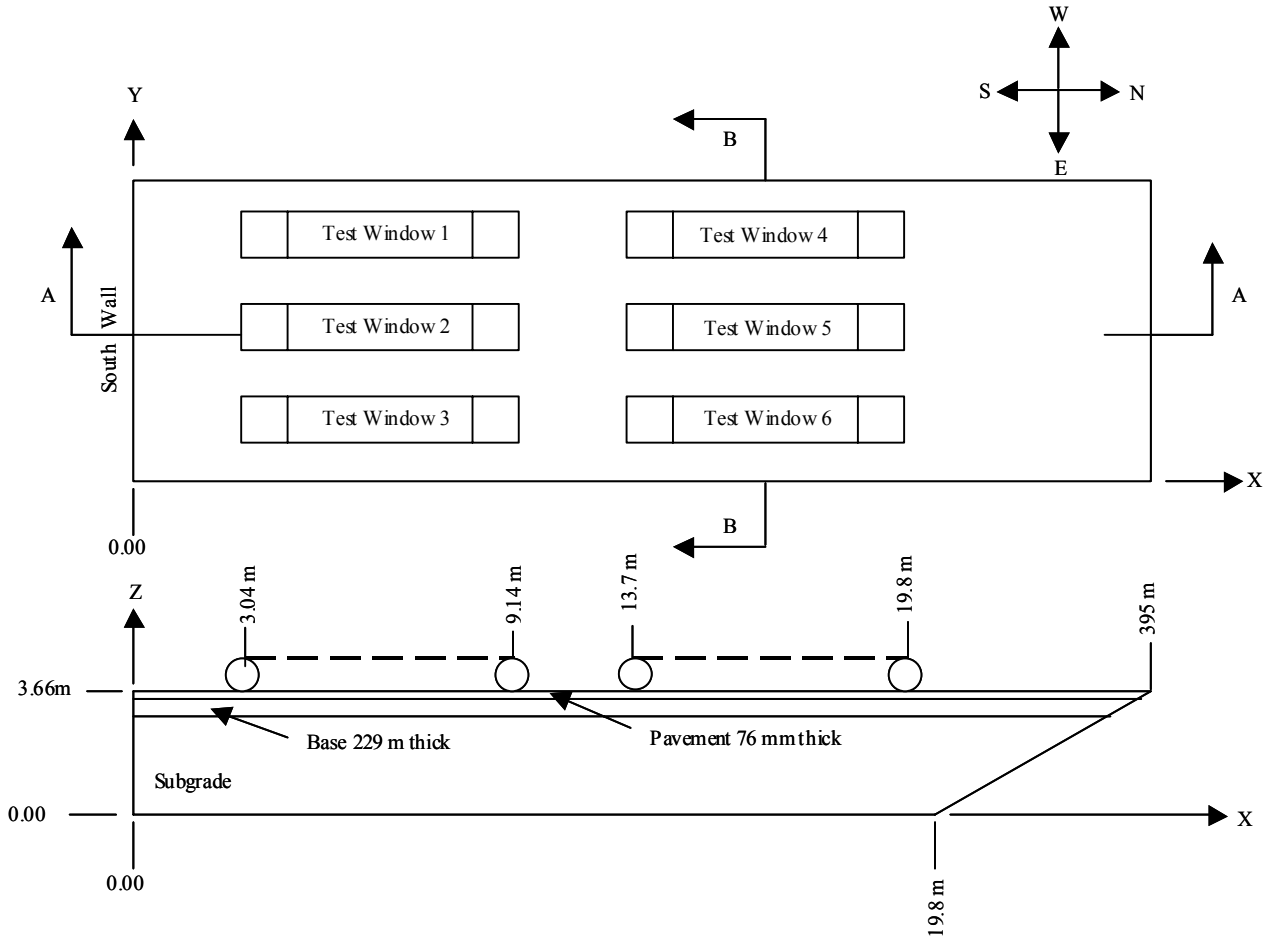

Figure 1.a. Plan view and longitudinal cross section of test section.

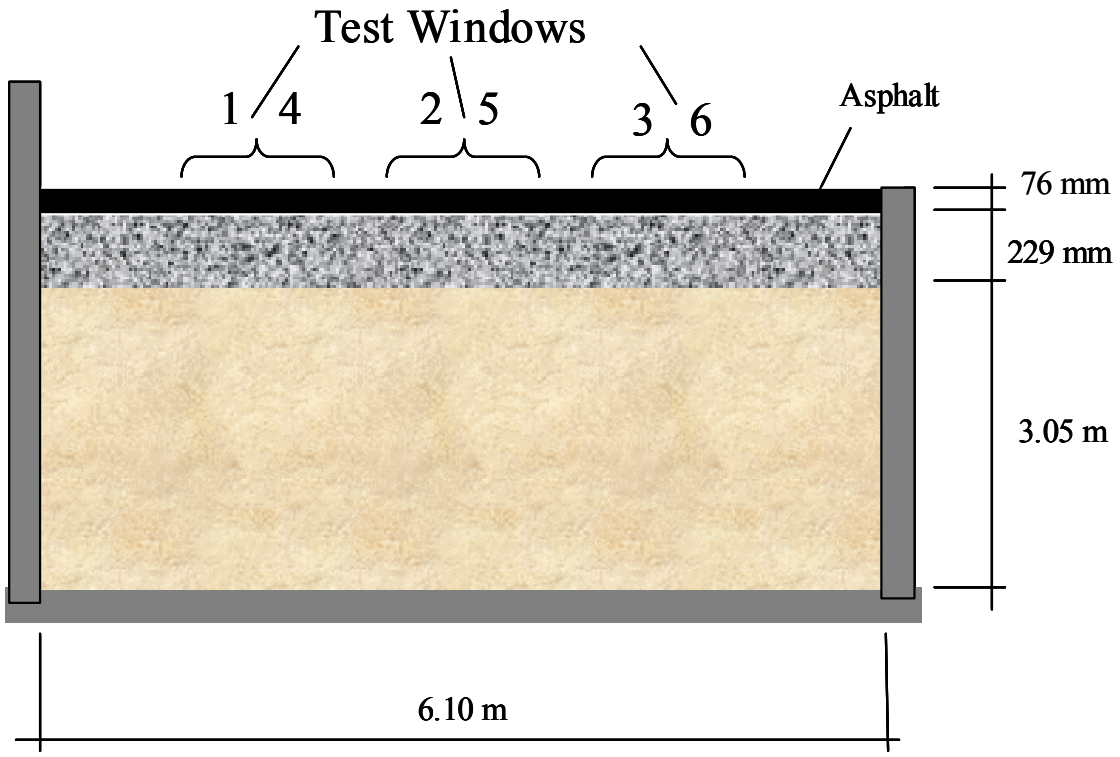

Figure 1.b. Transversal cross section.

3 MATERIAL PROPERTIES

Optimum moisture-density, grain size distribution, specific gravity, and liquid and plastic limits, and hydrometer tests were conducted in the laboratory on samples of the subgrade soil and the base course soil. Figure 3 shows grain size distributions for the subgrade soil and for the base course soil. The subgrade soil has approximately 85% passing the 0.074-mm sieve. The average liquid limit (LL) and plasticity index (PI) of the soil was 28% and 8% respectively. The average specific gravity was 2.72. According to the American Association of Highway & Transportation Officials (AASHTO) soil classification system, the subgrade soil was type A-4. According to the Unified Soil Classification System, the subgrade soil was type CL (low liquid limit clay).

The base course material was made of unbound crushed stone. It was classified as an AASHTO type A-1 soil. According to the Unified Soil Classification System, the base course soil was type GP-GM (mix of poorly graded gravel and silty gravel). About 10 percent by weight of the base course soil particles passed through the sieve 0.074-mm (#200) sieve. The fines in the base course material were classified as non-plastic.

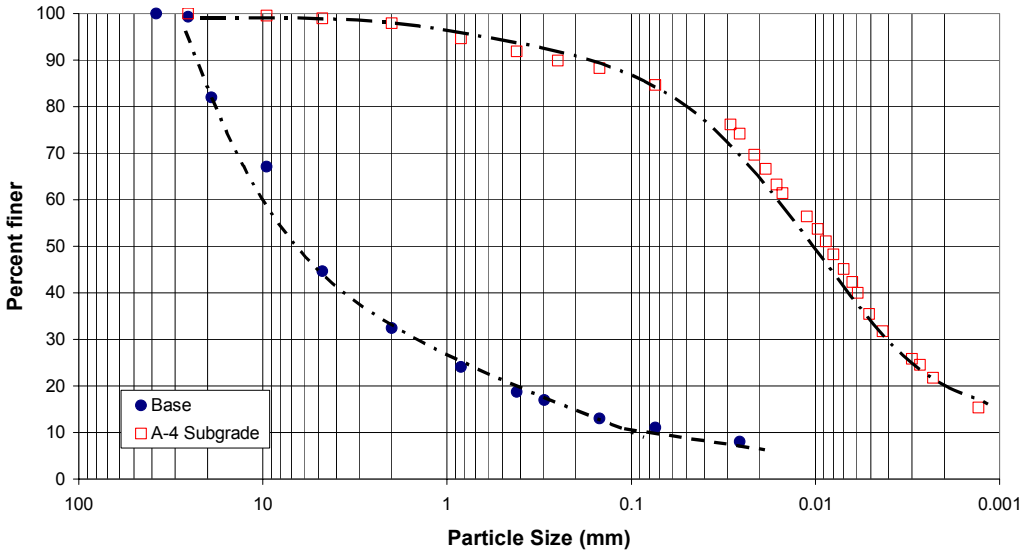

Figure 2. Subgrade and base course soil grain size distribution.

Optimum moisture content and maximum density tests were conducted on the subgrade material in the test section using the AASHTO test procedure, "*The Moisture-Density Relations of Soils Using a 5.5 lb (2.5 kg) Rammer and a 12 in. (305 mm) Drop* (T 99-90)". Samples were collected from various parts of the stockpile for the test and the results from these tests are shown in Figure 3. The optimum density and moisture content was 1778 kg/cm^3 and 16.5%respectively.

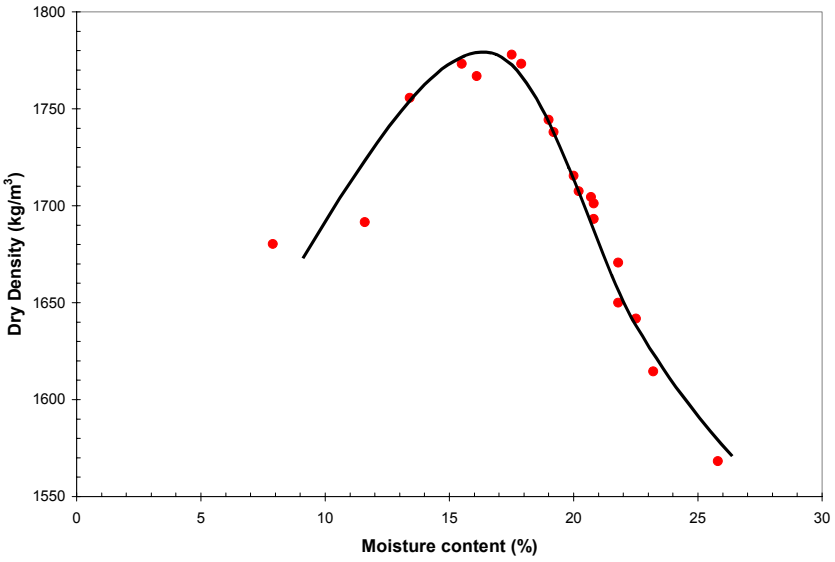

Figure 3. Moisture-Density relationship for A-4 subgrade soil

Table 2. Summary of classification test on the subgrade soil used in Test Section 705.

AASHTO	A-4
USCS	CL
Spec. Gravity	2.72
LL (%)	28
PI	8
Optimum moisture content (%)	16.5
Maximum Density (kg/m^3)	1780
% passing #10	98
% passing #200	85

The standard and modified moisture density relationships for the base material using the AASHTO T-99 and AASHTO T-180 are presented in Figure 4.

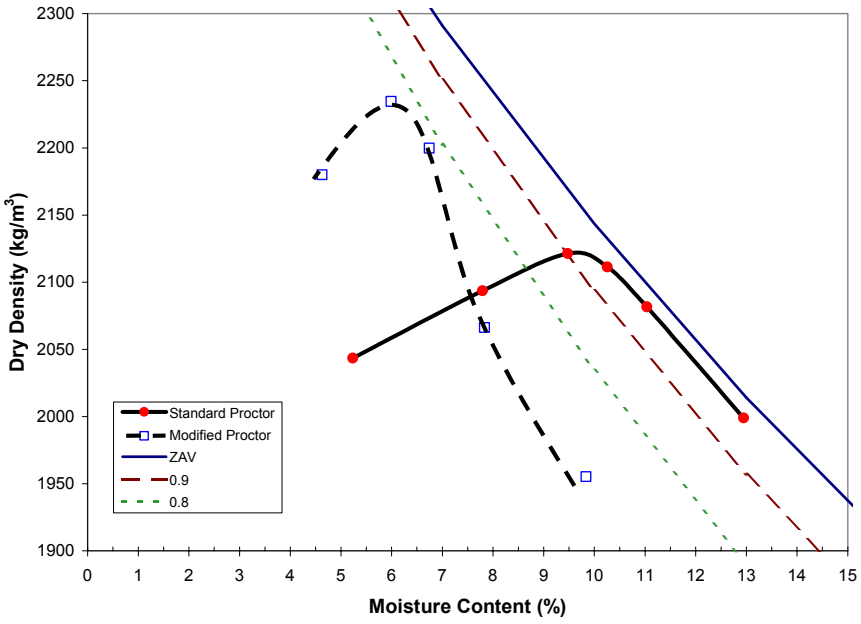

Figure 4. Moisture-Density relationships for base course

The optimum densities and moisture contents from the Standard and Modified Proctor tests are 2120 kg/m^3 and 9.5% and 2235 kg/m^3 and 6.0% respectively.

The asphalt mix was produced according to New Hampshire Type C specification. The Type C specification requires 95-100% passing the 12.52-mm (1/2-in.) sieve size.

The asphalt mix was produced according to New Hampshire Department of Transportation (NHDOT) Type C specification. The Type C specification requires 95-100% passing the 12.52-mm (1/2-in.) sieve size.

The asphalt concrete was placed and compacted in a single layer. Because of the soft subgrade soil, large pavement deformations were anticipated. Experience from previous experiments indicated that, under these conditions, delamination of asphalt layers is likely. The single layer construction was designed to prevent delamination.

The asphalt mix was produced according to New Hampshire Department of Transportation (NHDOT) Type C specification. The Type C specification requires 95-100% passing the 12.52-mm (1/2-in.) sieve size. The asphalt binder used conformed to specification PG64-22 with asphalt content of 6.1% by weight. . Nebraska Department of Roads Materials and Research Testing Laboratories conducted additional tests on the asphalt concrete. The test results are presented in a letter report in Appendix C.

4 CONSTRUCTION

The subgrade material was preprocessed to remove stones and to mix it well in a dry condition. The dry soil was brought into the test basin by means of a front loader. It was spread with a bulldozer in separate layers each about 0.15 m (6 inches) thick. Water was sprinkled onto the soil and sampled periodically. If the moisture content of the subgrade soil was found to be too dry, the soil was roto-tilled, and more water was added. When the target moisture content was achieved, the exiting subgrade surface was roller compacted with two passes of a 10-Ton (9,072-kg) steel roller in static mode.

Figure 5. Bulldozer spreading and grading the subgrade soil.

Moisture and density quality control measurements were taken at every other subgrade soil layer, i.e., every 0.30 m (1 ft).

Laboratory CBR tests were conducted to build a correlation between CBR and moisture content for the subgrade soil. This correlation provided a means to indirectly monitor CBR values during construction by monitoring the soil moisture content.

The subgrade soil was conditioned to gravimetric moisture content of about 23 percent. For this subgrade soil, this moisture content was as high as it could be built. Figure 6 shows that, for the target moisture content of the subgrade soil, the CBR value is about 1. The constructed subgrade was noticeably soft and it deformed easily under construction traffic.

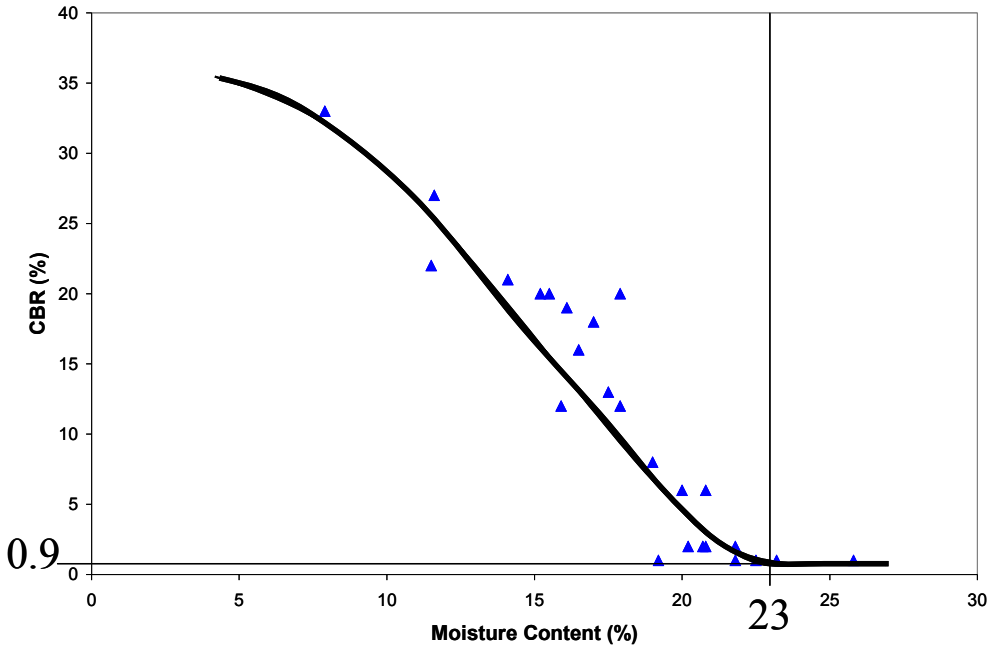

Figure 6. CBR-moisture correlation for the A-4 test soil.

The A-4 subgrade soil at the designed moisture content for this test section was extremely soft. It was difficult to produce a flat finished surface because the construction traffic would easily indent the soil as shown in Figure 7a and 7b. Even after placing and compacting the base course, significant deformations under construction traffic were easily noticeable.

Figure 7a. Soft subgrade soil surface after rolling.

Figure 7b. Construction equipment tire marks on subgrade soil.

At various depths, sensors were embedded into the soil and wires routed through recorded paths to reach the inlets leading to the instrumentation tunnel.

Figure 8. Installing sensors into the subgrade.

A single layer of asphalt concrete was place on top of the base course material. The hot mix asphalt (HMA) was produced at a local asphalt plant about 7 miles from the test sections site. The asphalt concrete mix was transported in dump trucks. A Black Knox® paver model PF-400A was used to place the asphalt in a single layer over 2 lanes. A single layer was chosen instead of the traditional 2-layer system to avoid the possibility of interlayer delamination. Recent experience with pavement test sections built with similarly soft soils indicated that a 2-layer asphalt system is prone to delamination and premature asphalt shear failure due to large pavement deflections.

Figure 9. Construction loads caused significant ruts during the asphalt paving operation.

The air temperature during the asphalt paving operation was about 10°C (50°F). The average temperature of the asphalt mix when deposited on the paver hopper was 148°C (298°F). Immediately after placing, the asphalt mixture was at an average temperature of 130°C (266°F). Roller compacting took place as soon as the asphalt paver had completed each lane.

Compaction of the asphalt concrete was done using a Bomag® steel roller model BW 120 AD-3. The steel roller applied 4 passes in static mode plus 4 passes in vibratory mode. The roller operator noted that it was difficult to smooth the surface because the pavement structure was very soft.

The soft subgrade soil impacted the stability of the base course. The paver tracks and the dump truck tires caused the development of ruts on top of the base course. These ruts were filled with asphalt concrete during paving. This resulted in large variations of the asphalt layer thickness. From the records of the total volume of asphalt concrete transported into the test sections, it could be established that the average thickness of the asphalt layer was 100 mm (3.9 inches). The planned thickness was 76 cm (3 inches).

Backscattered nuclear gauge density measurements were taken at various locations on top of the finished asphalt pavement to try to define the asphalt thickness variations. Because the nuclear gauge results were not conclusive, a series of cores of 51 mm (2-inch) in diameter were taken. Figure 10 shows the asphalt thickness results. The thickness variations are very significant.

The test windows were paint-marked on the finished asphalt pavement in preparation for testing with the heavy vehicle simulator.

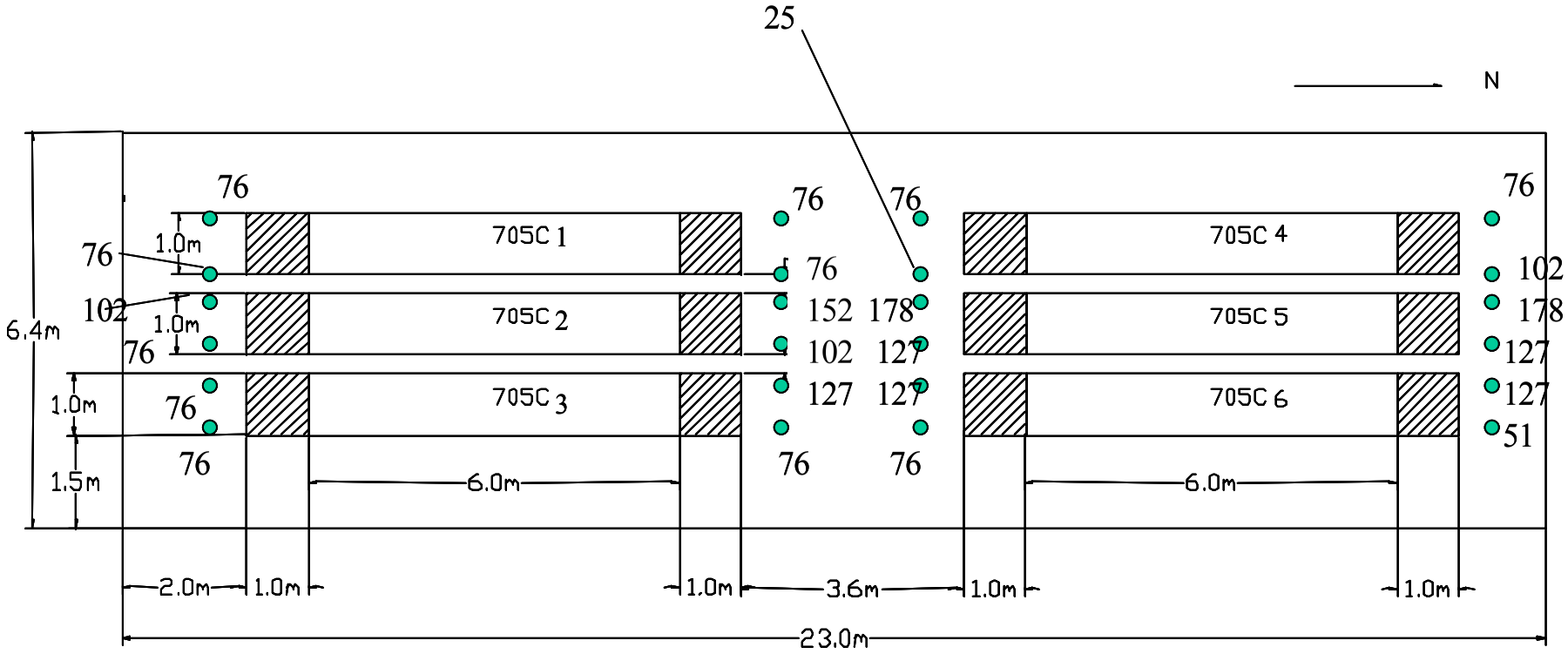

Figure 10. Asphalt concrete thickness in millimeters measured on cores taken at the corners of each test window.

Construction Quality Control

Once the compaction was completed for each soil layer, a series of tests were conducted. These measurements were made on every 300-mm lift. The tests included determination of moisture, density, Vane shear, and layer thickness. The primary properties used for construction quality control was the moisture content.

Moisture Content

Moisture and density measurements were taken using a Troxler nuclear gage at the locations shown in Figure 11. The moisture and density determinations on the subgrade layers were made in a volume of soil using the direct approach. The probe from the nuclear gage penetrated into 150 mm of soil. On each lift, 30 measurements of moisture and densities were made. A total of 120 moisture and density measurements were made during the construction of the subgrade. Moisture and density measurements were also conducted on top of the finished base course using the backscattered method.

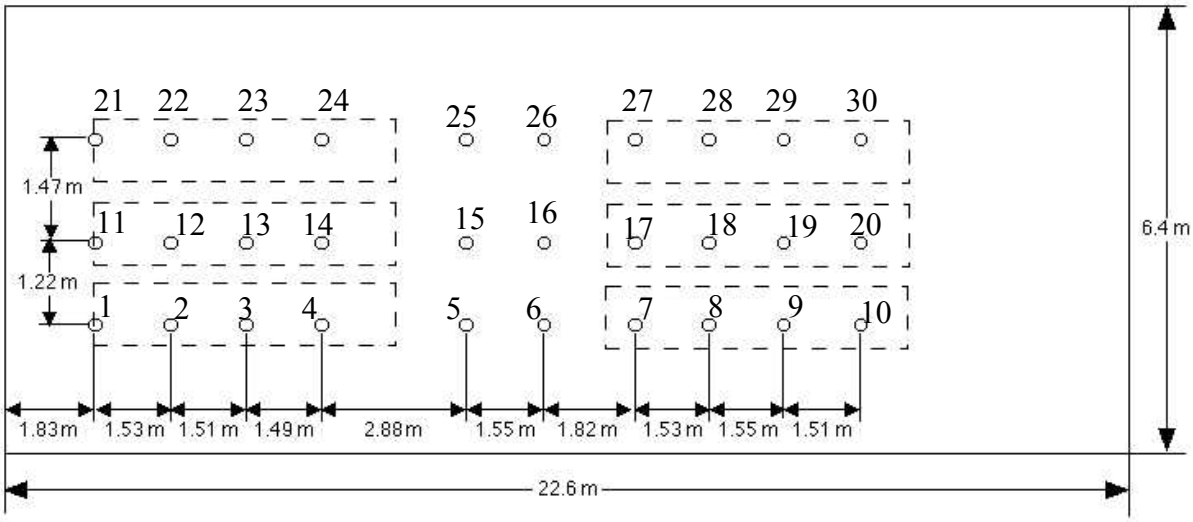

Figure 11. Locations of moisture and density measurements on Test Section 705.

(See detailed measurements in Appendix B).

In addition to the nuclear moisture and density tests, oven dry verifications were conducted. Figure 12a shows a histogram of 120 moisture content measurements conducted at various locations within the subgrade. Figure 12b shows a histogram of 18 oven dry verifications.

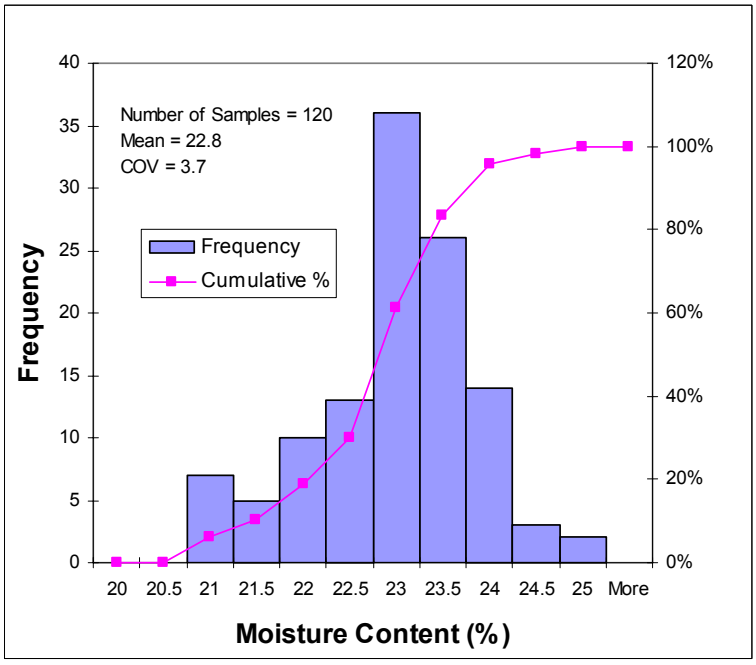

Figure 12a. Histogram of gravimetric subgrade soil moisture measurements by means of a nuclear gage.

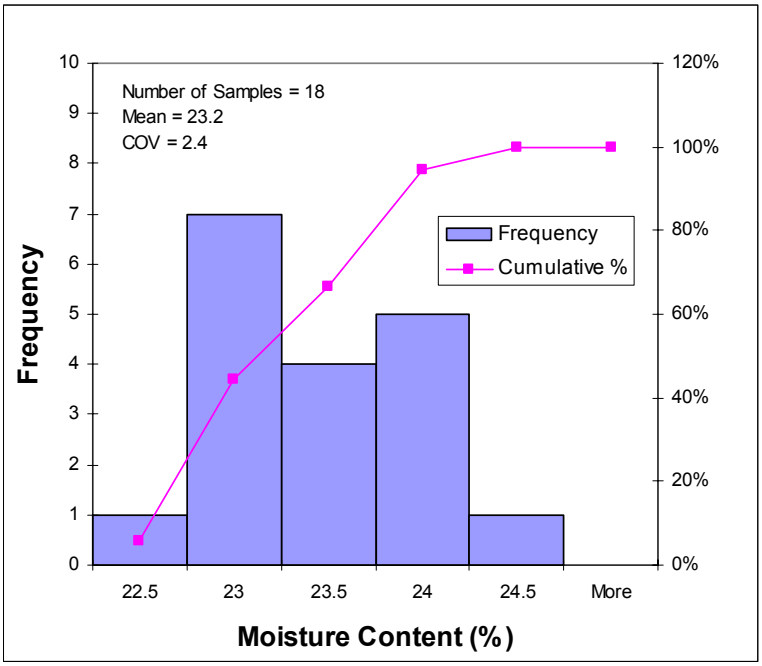

Figure 12b. Histogram of gravimetric subgrade soil moisture measurements by the oven dry method.

The average moisture content of the subgrade soil during construction was 23 percent. At this moisture content, the soil was very soft. When construction traffic was applied, the soil yielded in a visco-plastic manner. Significant ruts developed on the base course.

Nuclear gage moisture and density measurements were taken at 30 locations on the base course. The test locations are the shown in Figure 11. A histogram of the test results is presented in Figure 13. The mean moisture content in the base course obtained with the nuclear gauge coincided with the optimum moisture content established through oven dry laboratory tests, i.e., 3.3 percent. However, the dispersion of the data was larger with the nuclear gauge. This data dispersion is typical of nuclear gage measurements on granular materials.

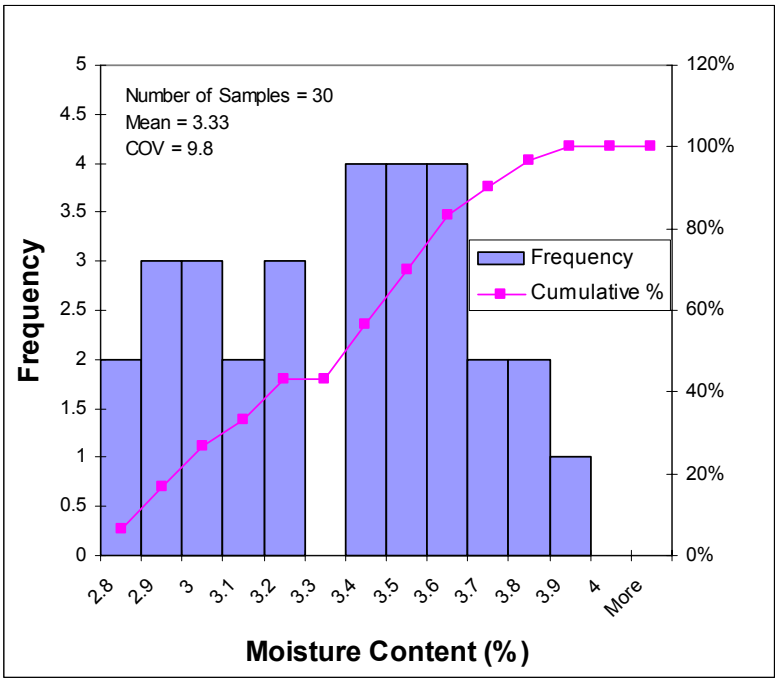

Figure 13. Histogram of gravimetric moisture measurements on the base course by means of a nuclear gage.

Dry Density

Density tests were conducted in the subgrade soil and on the base course using a nuclear gage. For the subgrade layers, the direct method was used, i.e, the radioactive source inserted into the soil about 0.15 m. For the base course, the backscattered method was followed.

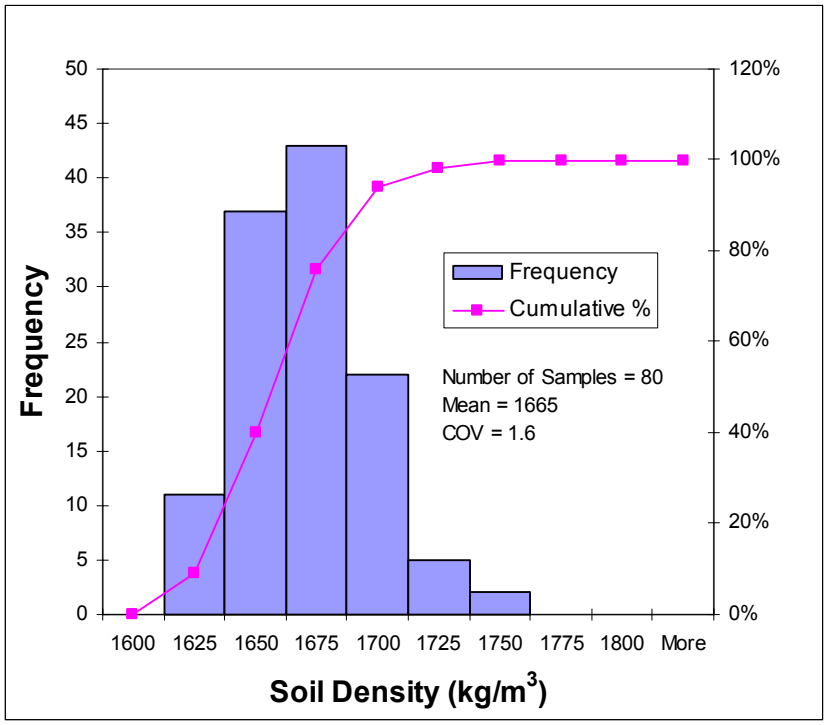

Figure 14. Subgrade soil density measurements at 120 locations.

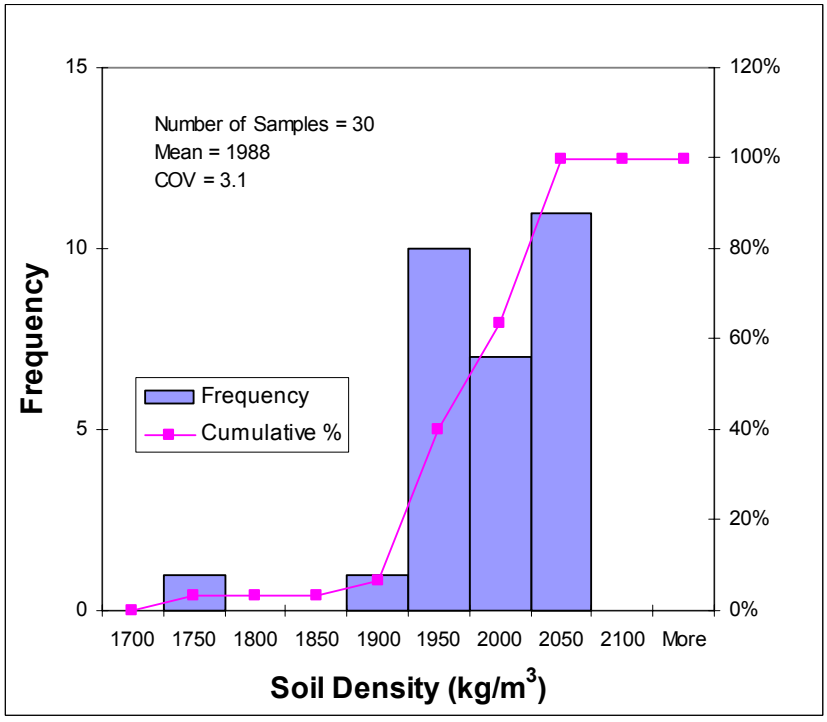

Figure 15. Base course density measurements at 30 locations.

The mean dry density of the subgrade was 1665 kg/m ^{3} (104 lb/ft ^{3}), with a coefficient of variation (COV) of 1.6 %. A histogram and cumulative frequency plot of the subgrade soil dry density during construction is presented in Figure 14.

The mean dry density of the base course was 1988 kg/m^3, with a coefficient of variation (COV) of 3.1 %.

Vane Shear

Clegg hammer tests were attempted in the subgrade soil but the results were meaningless because the soil was too soft. Vane shear tests were conducted instead of the Clegg hammer tests because this instrument is more reliable with soft soils.

Vane shear tests were conducted at 36 locations at the top of the subgrade and at depths 0.08 m, 0.39 m, 0.69 m and 0.99 m from the top of the subgrade. This resulted in 144 measurements. Figure 16 shows the location of the shear tests on a soil layer. Figure 17 presents a histogram of the Vane shear readings at all 144 test points.

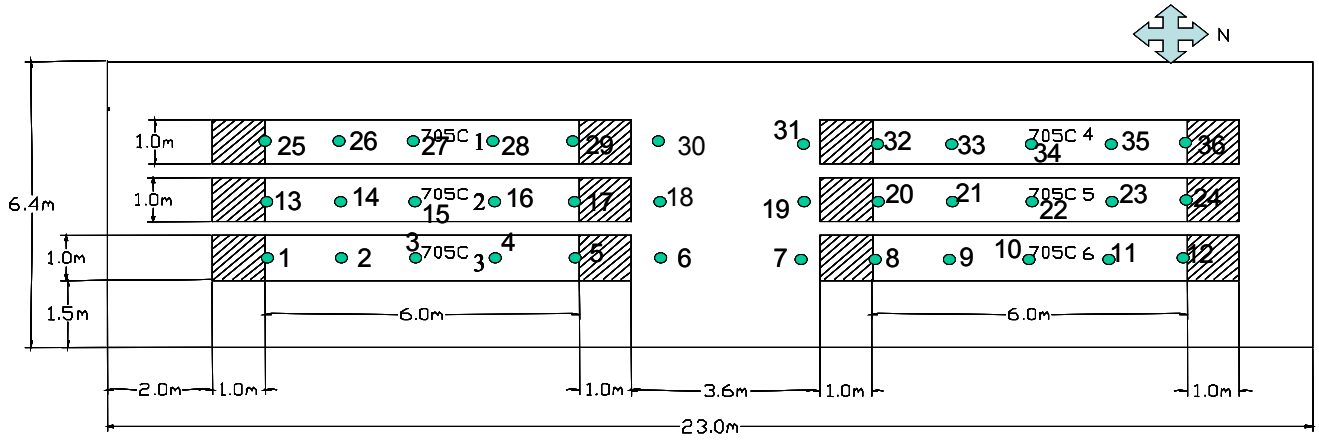

Figure 16. Locations of Vane shear measurement points.

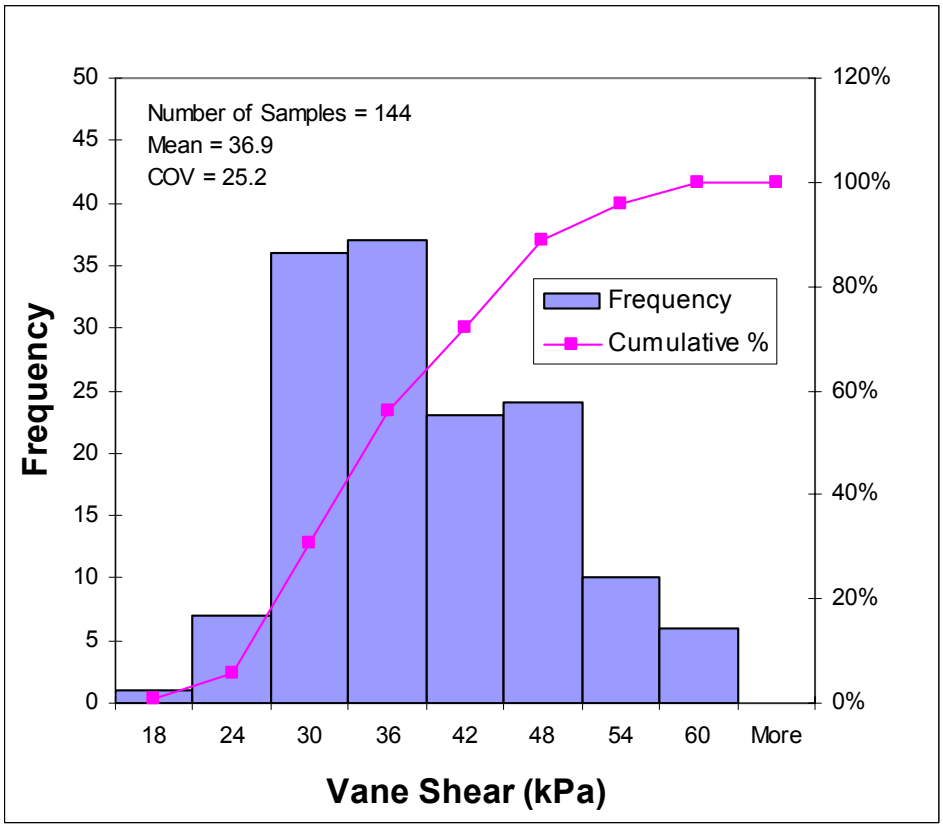

Figure 17. Histogram of Vane shear measurements in the subgrade.

The coefficient of variation (COV) of this set of measurements was relatively high. This may be due to the presence of small aggregate particles in the shear cylinder. The mean shear was 36.9 kPa. Low shear resistance is indicative of a very soft soil.

Falling-Weight Deflectometer Tests

A series of falling-weight deflectometer (FWD) tests was conducted on each constructed test window prior to HVS testing by means of a Dynatest FWD. The tests were conducted at 14 stations spaced every 0.61 m (2ft) along the tire path for each test window. Four drop heights with 4 repetitions at each drop height were used in the test. No FWD measurements were taken at the end of the test, as the pavement surface was severely deformed.

The data was processed by means of the Corps of Engineers Layer Elastic Evaluation Program (LEEP). Given the AC thickness variability in this test section, only the data from station number 8 was used for each window. The thickness for this location was directly measured in trenches during the forensic evaluation.

The backcalculation program in LEEP is WESDEF. The program is able to backcalculate up to 4 layers, and automatically places a rigid layer at the bottom of the subgrade. This is fine with our results as there was a concrete floor at the bottom of the subgrade.

Backcalculation of FWD data

The backcalculation program in LEEP is WESDEF. The program is able to backcalculate up to 4 layers, and automatically places a rigid layer at the bottom of the subgrade. This is fine with our results as there was a concrete floor at the bottom of the subgrade. FWD measurements were taken on each test window prior to HVS testing. A total of 14 FWD tests were conducted on each test window. Four drop heights with 4 repetitions at each drop height were used in the test. No FWD measurements were taken at the end of the test, as the pavement surface was severely deformed.

Due to the extreme weakness of the subgrade, AC cores were taken at various locations in the test section. The thickness of the cores and results from the forensic study were used to determine the thickness of the AC and subsurface layers. These thickness values are presented in Table 3. The thickness values of some of the layers were further adjusted to reduce the error in the backculation process. These values are shown in parentheses in Table 2.

Table 3. Pavement layer thickness used in backcalculation process.

Test Window	Layer Thickness (mm)			
	AC	Base	Test Subgrade	Lower Subgrade
705C1	89	241	1219	1499
705C2	147	211	1219	1471
705C3	81	236	1219	1511
705C4	71	191	1219	1567
705C5	188 (178)	234 (178)	1219 (1397)	1407 (1296)
705C6	79	231	1219	1519

A representative location corresponding to the forensic trench location was selected for each test window. The selected location was FWD station 8. The FWD data was normalized to 36-kN. The normalized deflections are presented in Table 4. The reason for 36-kN and not 40-kN was that in some windows, if 40-kN was used, the deflections had to be extrapolated. Table 5 shows the seed, minimum, maximum and Poisson's ratio values used in the backcalculations. The rigid layer modulus is automatically set by the program to 10342 MPa.

Table 4. Normalized deflections at station 8 and load of 36-kN.

Test Window	Deflection (micron)						
	D1	D2	D3	D4	D5	D6	D7
705C1	1194	815	458	285	162	78	26
705C2	527	443	338	245	163	98	51
705C3	1770	1251	645	330	139	44	30
705C4	975	638	374	262	174	104	52
705C5	307	266	215	167	120	79	46
705C6	867	629	387	257	161	96	48

Table 5. Initial and seed modulus used for the various layers.

Material	Modulus (MPa)			Poisson's ratio
	Seed	Min	Max	
AC	2758	690	6900	0.35
Base	207	7	1030	0.35
Test Subgrade	69	7	103	0.4
Lower Subgrade	69	14	165	0.4
Rigid layer	10342	10342	10342	0.15

The program also provides an initial seed modulus for the subgrade, based on the outer deflection data. This can be used or reset by the user.

The results from the backcalculation process are presented in Table 6. We found that we had to adjust the asphalt modulus manually to reduce the error between the backcalculated and measured deflections. In some cases, although, the error appears to be acceptable, the backcalculated modulus does not appear to be reasonable. This was especially true with the base course.

Table 6. Backcalcualted layer moduli.

Test Window	AC	Base	Test Subgrade	Lower Subgrade	Error (%)
705C1	2823	146	15	97	26
705C2	5171	382	15	165	2.7
705C3	4654	13	20	39	9.9
705C4	2758	190	27	26	5.5
705C5	5516	1034	25	113	3.8
705C6	4096	254	23	35	2.5

5 INSTRUMENTATION

The test section was instrumented with the following sensors:

- Ɛmu coils
- Stress cells:

  Dynatest® in the subgrade soil

  Geokon® in the base course
- Thermocouples
- Moisture sensors

Ɛmu Coils

Ɛmu coils were installed to measure deformation between pairs of coils. This enables calculation of the strains in the vertical (z), longitudinal (x), and transverse (y) directions at various locations within the pavement structure. Figure 18 shows a set of εmu coils that enables triaxial measurements. Each εmu coil is 100 mm in diameter. During measurements, εmu coils work in pairs: one transmitter and one receiver. Their transmit-receive function can be alternated. The timing and order of measurement of each pair must be carefully designed to avoid interference among coil pairs.

Figure 18. Ɛmu coils

When an alternating current is passed through a εmu coil, an alternating magnetic field is generated. Another coil placed within this field will have an alternating current induced in it. The magnitude of the induced current is proportional to the magnitude of the exciting current and the distance between the transmitter and receiver coils. The magnitude of the transmitter coil can be kept constant therefore changes in the magnitude of the current in the receiver coil are attributed to a change of distance between the coils. Prior to installation into the test sections each coil pair is individually calibrated to produce a correlation between current and distance. Fifty eight coil pairs where installed in each test window for a total of 348 coil pares for the six test windows included in this test section. They were installed at various locations in the base course and in the subgrade under the wheel path. The εmu coils in the base course and the upper subgrade were replicated to enhance reliability.

The wires from the εmu coils are routed to a data logger that measures the voltage of receiver coils at a rate of 400 Hertz for 3 seconds. A proximity switch controls the start of the data collection for a given coil pair.

One difficulty in measuring dynamic displacement under moving wheels with εmu coil is that they register the combined effect of displacement and a magnetic field generated by movement of steel (a magnetic material) in the tire assembly near the coils. This difficulty is resolved by measuring the signal generated in the εmu coils while the tire assembly is moved along the traffic path suspended in the air near the pavement surface but without touching the pavement (no load passes). The signal generated in this manner is subtracted from the signal generated in the receiving coils during the actual traffic passes.

Equation 1 contains a function that correlates receiver coil voltage to distance in millimeters between two coils.

$$D = a\ V^{n} \qquad \text{Equation 1.}$$

where D = static distance between the transmit and receive coils
V = demodulated (d.c.) "static" voltage from the coils
a and n = regression constants for a pair of coils.

The coefficients *a* and *n* are determined for each pair during laboratory calibration for each coil pair.

Stress Cells

A triaxial set of 3 Dynatest® stress cells was installed in the subgrade in each of the six test windows at a depth of 76 mm (3 in.) from the top of the subgrade. An additional triaxial set of Dynatest® stress cells was installed at a depth of 223 mm (9 in.) from the top of the subgrade in each of Test Windows 2 and 5.

The raw voltage signal obtained from the stress cells is converted into engineering units of stress by means of the following equation:

$$\sigma(kPa) = \frac{(1000 \times V)}{(V_{ex} \times Gain \times GF \times 10^{-5})} \qquad \text{Equation 2.}$$

where σ = measured stress

V = measured voltage

V_{ex} = excitation voltage

GF = gain factor

Gain = A/D card gain

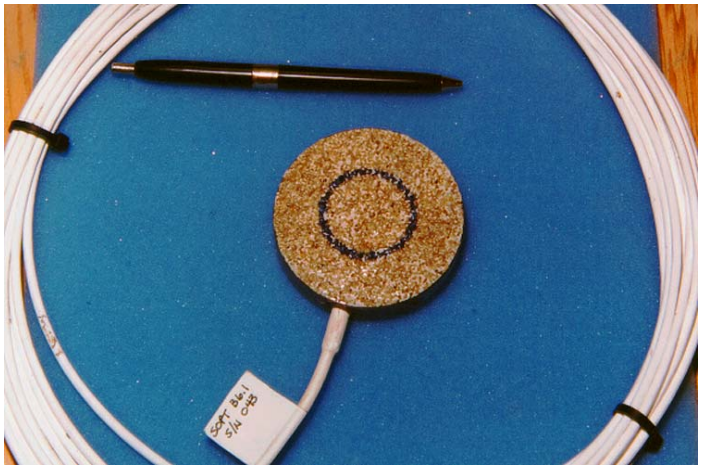

Figure 19. Dynatest® stress cell.

Dynatest stress cells were used in the subgrade because of their good reliabity and negligible hystherisis. They were not used in the base course because of their small size in proportion to the maximum particle size.

Geokon® stress cells were embedded in the middle of the base course at Test Windows 2 and 5. These stress cells were chosen because of their larger diameter (223 mm or 9 in.). Their voltage to stress correlation is linear and the intercept is zero.

$$\sigma = 40\ V \qquad \text{Equation 3}$$

where

σ = measured stress

V = measured voltage

Figure 20. Geokon® stress cell.

During the traffic testing of the test windows, the heavy vehicle simulator recorded the applied load for each pass. The output of the stress cells was also recorded for a number of passes at various stages. Sensor output was recorded every time the tire moved 8.34 mm along the traffic path. An analysis of the stress bulb generated over the stress cells enabled in-situ verifications of the accuracy of the sensor and data acquisition output.

Thermocouples

Subsurface temperatures were taken at various depths in the subgrade, the base course and the asphalt concrete using thermocouple sensors. The thermocouples have an accuracy of ± 0.5°C. The temperatures were recorded every 4 hours during the duration of the traffic tests. Two sets of eight thermocouples each were installed at locations representative of the test windows.

Moisture Sensors

Three sets of Vitel Hydra® moisture sensors were installed at three representative locations in the test section for a total of 9 sensors. Each set of 3 moisture sensors had one sensor in the base course at a depth of 10 cm (4 in) above the top of the subgrade. The second sensor was located at the top of the subgrade, and the third sensor was located at a depth of 30 cm (1 ft.) from the top of the subgrade.

Vitel Hydra probes measure moisture soil content indirectly by measuring the dielectric constant of the soil at a frequency of 50 MHz. The measured dielectric constant is divided into its two components: capacitive and conductive. The capacitive component depends on the volumetric moisture content of the soil. The dielectric constant of bulk water at 20°C and 1 atmosphere is 80.2 (Lide, 1994). The dielectric constant of dry soil is typically in the order of 3 to 4 depending on the mineral constitution of the soil. Through the use of appropriate calibration curves, the dielectric constant measurement can be related to soil moisture. The accuracy of the volumetric moisture content is ±2% using the calibration equations provided by the manufacturer. The accuracy is increased to ±0.5% if calibrations are conducted with the test soil. The reproducibility of the measurements is ±0.3%. The reliability of the data deteriorates below –10°C but the current experiment was well above that temperature.

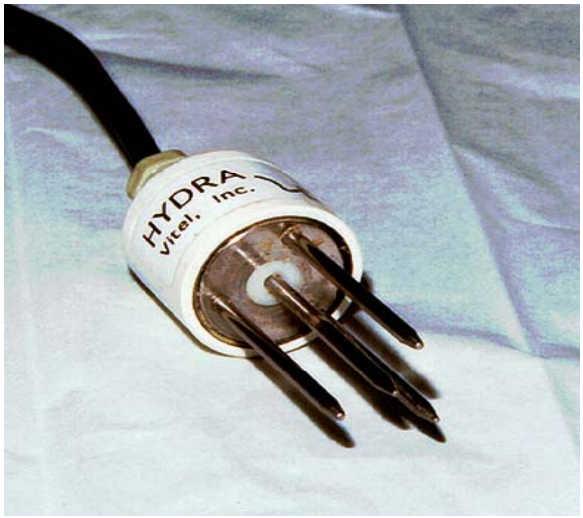

Figure 21. Vitel Hydra moisture sensor.

Data Acquisition System

The primary data acquisition system for this experiment was engineering specifically for this project because no suitable system was commercially available. This system was used to measure the response of stress and strain sensors. In order to avoid interference, the εmu coil pairs had to be read at different times than their neighboring sensors. The data acquisition system includes a set of relays to time the various measurements.

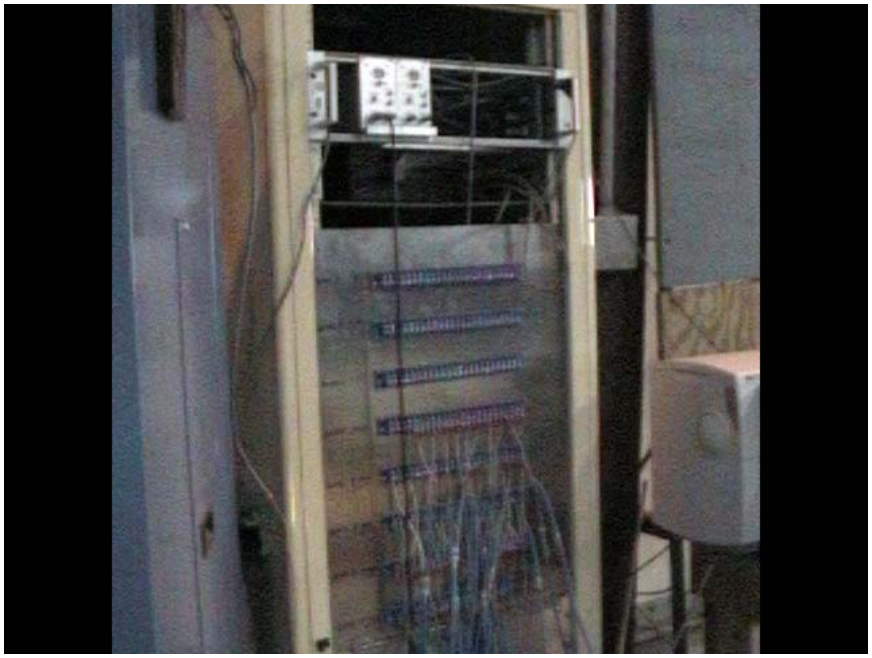

Figure 22. εmu relays and custom-made electronic hardware.

The primary data acquisition system was controlled by a dedicated personal computer that also stored the data. A computer program written in LabView® language was developed specially for the current instrumentation.

Figure 23. Computer that controlled the primary data acquisition system.

In addition, a Campbell Scientific® CR10X data logger equipped with multiplexers was programmed to collect data from moisture and temperature sensors embedded in the test sections.

6 ACCELERATED TRAFFIC TESTING

The test windows were subjected to accelerated loading using the Dynatest® Heavy Vehicle Simulator (HVS). A description of the HVS can be found in Appendix D. The tire assembly was a standard dual truck tire. The traffic speed was 12 km/hr (7.5 miles/hour). The traffic was allowed to wander across the 0.91-m (3 ft) width of the test windows. The tire pressure was set to 689 kPa (100 psi). The mean applied loads are summarized in Table 7.

Table 7. Prescribed traffic load for each test window.

Test Window	Load (kips)	Load (kN)
705c1	6	26
705c2	9	40
705c3	5	22
705c4	4	18
705c5	12	53

The following tests were conducted:

1. Transverse profile measurements of each test window were conducted using a laser profilometer shown in Figure 25. The laser source scans the surface on a straight line across the test window at approximately 9-mm intervals at 256 points per cross section. Twenty cross sections were measured along the tire path within a test window. The distances measured at zero pass level, i.e. before traffic is applied, are compared to the distances measured at all other pass levels. The supports of the profilometer are away from the test window enough to sustain the assumption of fixed spatial location. This assumption is checked with rod and level surveys, and adjusted if elevation changes are detected.
2. Level surveys were made during every test to determine whether the reference points (i.e. where the feet of the Profilometer were located during the surface profile measurements) moved. Surface profile measurements were made at each pass level when dynamic stress-strain measurements were taken for each test window. The maximum rut depth was calculated as the difference between of the surface profile after N passes and a baseline. The baseline was the measurement taken prior to loading of the test section. A typical surface rut measurement and the definition of maximum rut depth are shown in Figure 26. Testing was terminated when the average maximum surface rut depth of 12.5 mm (1/2 in) was reached or exceeded.
3. Subsurface stresses, strains, and permanent displacements were also measured in the vertical and in two perpendicular horizontal directions at various pass levels. Dynamic stress and strain measurements in the test windows were taken when the wheel was in the position shown in Figure 27.
4. Permanent deformation measurements were taken using the εmu coils while the tire assembly was static. A loose coil gage on the surface was used to measure the permanent deformation between the AC surface and the first coil in the base course.

Figure 24. The laser profilometer.

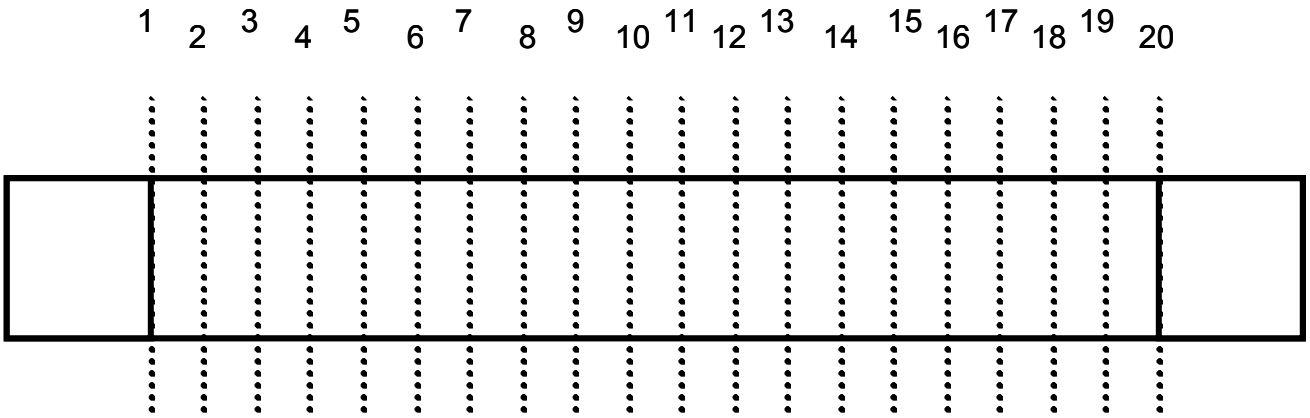

Figure 25. Locations for profile measurements in a test window.

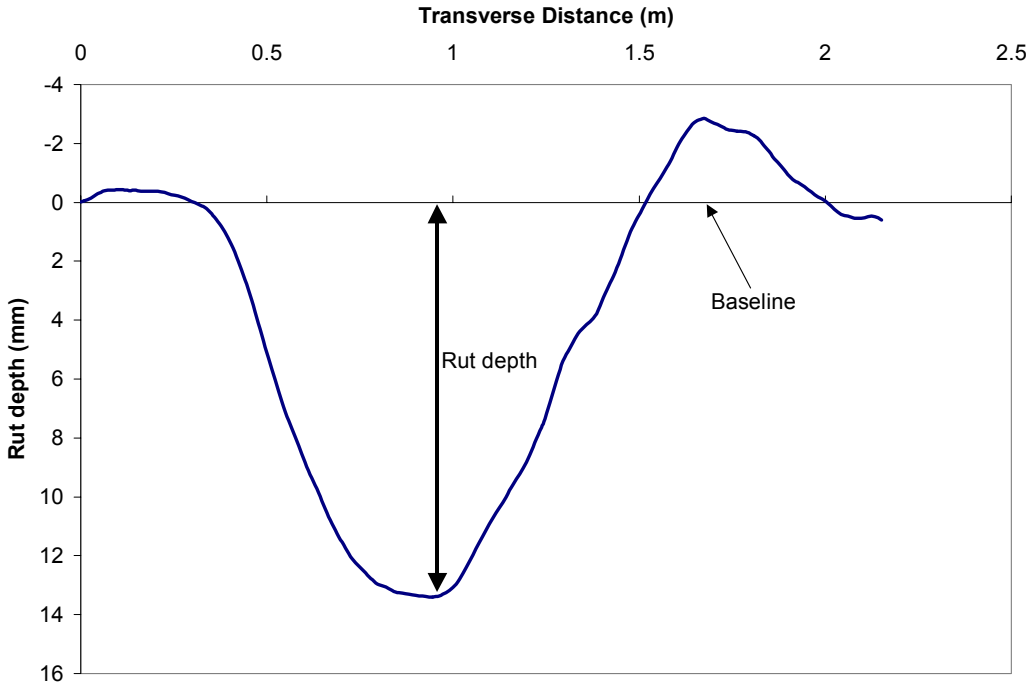

Figure 26. Definition of rut depth

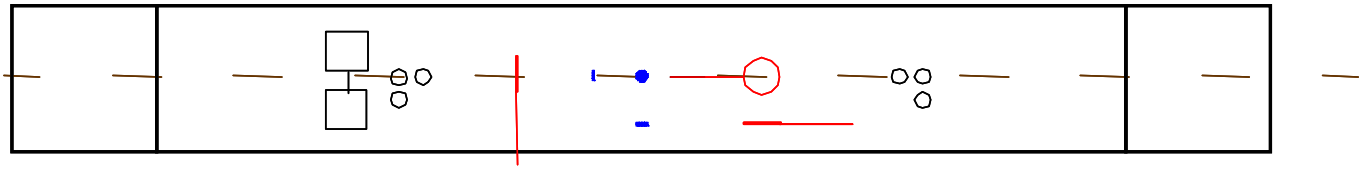

Figure 27. Location of test wheels during dynamic stress and strain measurements.

7 SUMMARY OF RESULTS

Actual Applied (HVS) Traffic Loads

The Heavy Vehicle Simulator HVS applied constant load along the effective test window. The applied load was recorded for each pass.

The tire assembly consisted of a standard dual truck tire. The traffic speed within the effective test window was kept constant at 12 km/hr (7.5 miles/hr). The traffic was allowed to wander across the 0.91-m (3-ft) width at 0.05-m (2-in.) intervals in a regular pattern from one side of the test window to the other, and back. Table 8 presents the mean load applied to each test window. These values slightly differ from the intended loads presented in Table 7. By design, the loads were varied from test window to test window. The tire pressure was kept constant at 689 kPa (100 psi).

Table 8. Actual Mean Applied Traffic Loads

Test Window	Load (kips)	Load (kN)
705c1	5.7	26
705c2	9.3	41
705c3	4.9	22
705c4	4.0	18
705c5	12.1	54

Temperatures During The Traffic Tests

The temperatures reported by thermocouples embedded at various depths within the base course and the subgrade are presented in Figure 28. Most of the pavement temperatures were kept in the range of 15-20 °C (59-68 °F). The small changes in temperatures such as those observed in Figure 28 suggest negligible effect in material properties.

Air and pavement surface temperatures were measured manually at each pass level for each test window. Table 9 displays the average temperature during the HVS testing.

Table 9. Manual readings of air and pavement surface temperatures during traffic tests.

	Average Temperature (°C)	
Test Window	Air	Pavement Surface
705c1	20	19
705c2	21	21
705c3	16	15
705c4	15	15
705c5	18	18

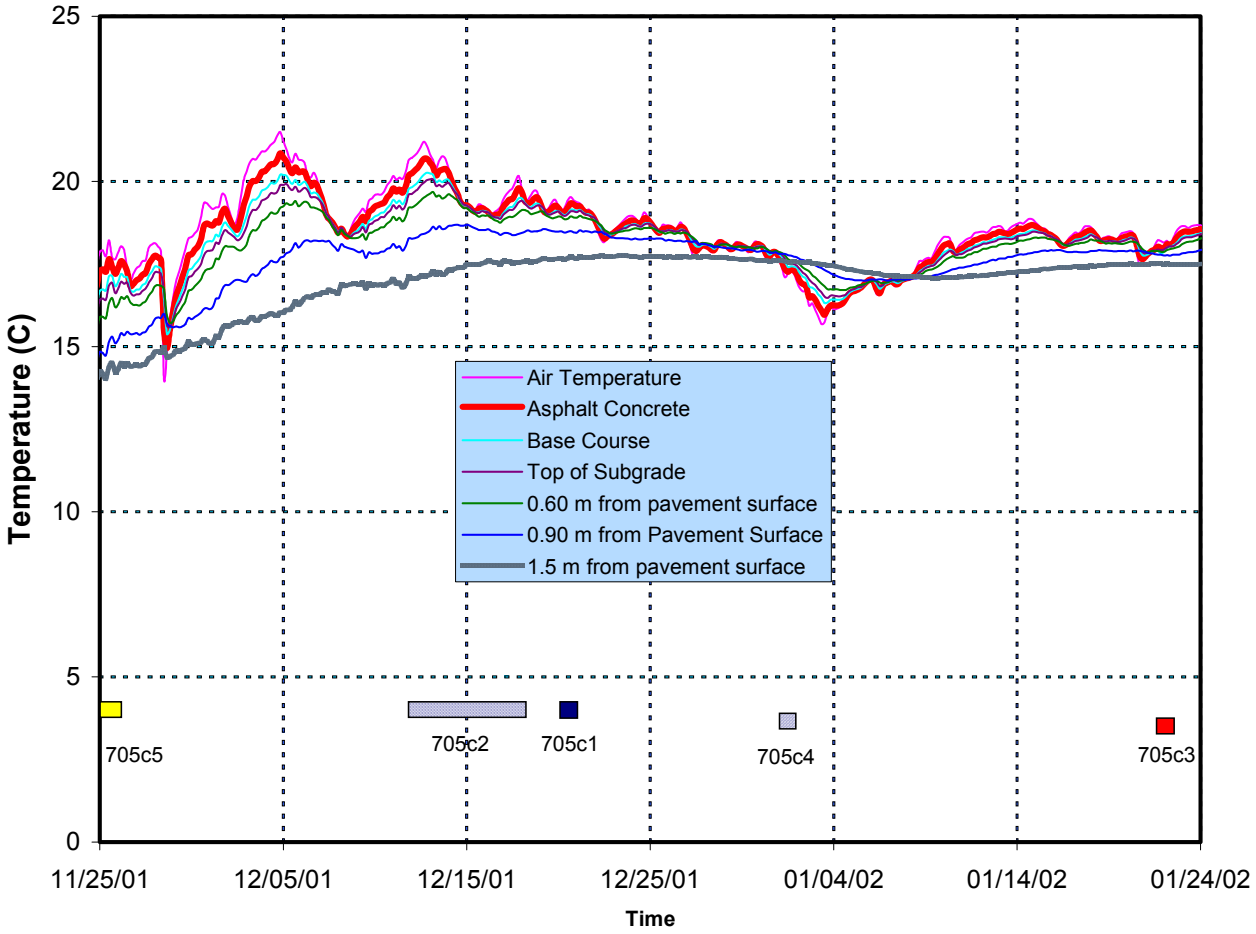

Figure 28. Pavement temperatures during the traffic tests.

Test window 705c6 was not tested because of severe damage extended from neighboring test window cracking and rutting.

Subgrade Moisture Content

Moisture content tests were taken during the construction of the test section at each soil layer. During the traffic test period, soil moisture data was recorded from embedded Vitel Hydra sensors. After the traffic tests had been completed, trenches were excavated and samples gathered to determine the moisture content at that stage. Figure 29 shows the moisture content regime for a region near the top of the subgrade from the construction through the traffic tests and at the forensic excavations. Figure 29 suggests that some drying occurred throughout the process. However, the soft subgrade soil manifested throughout the traffic tests in the form of large resilient and permanent deformations.

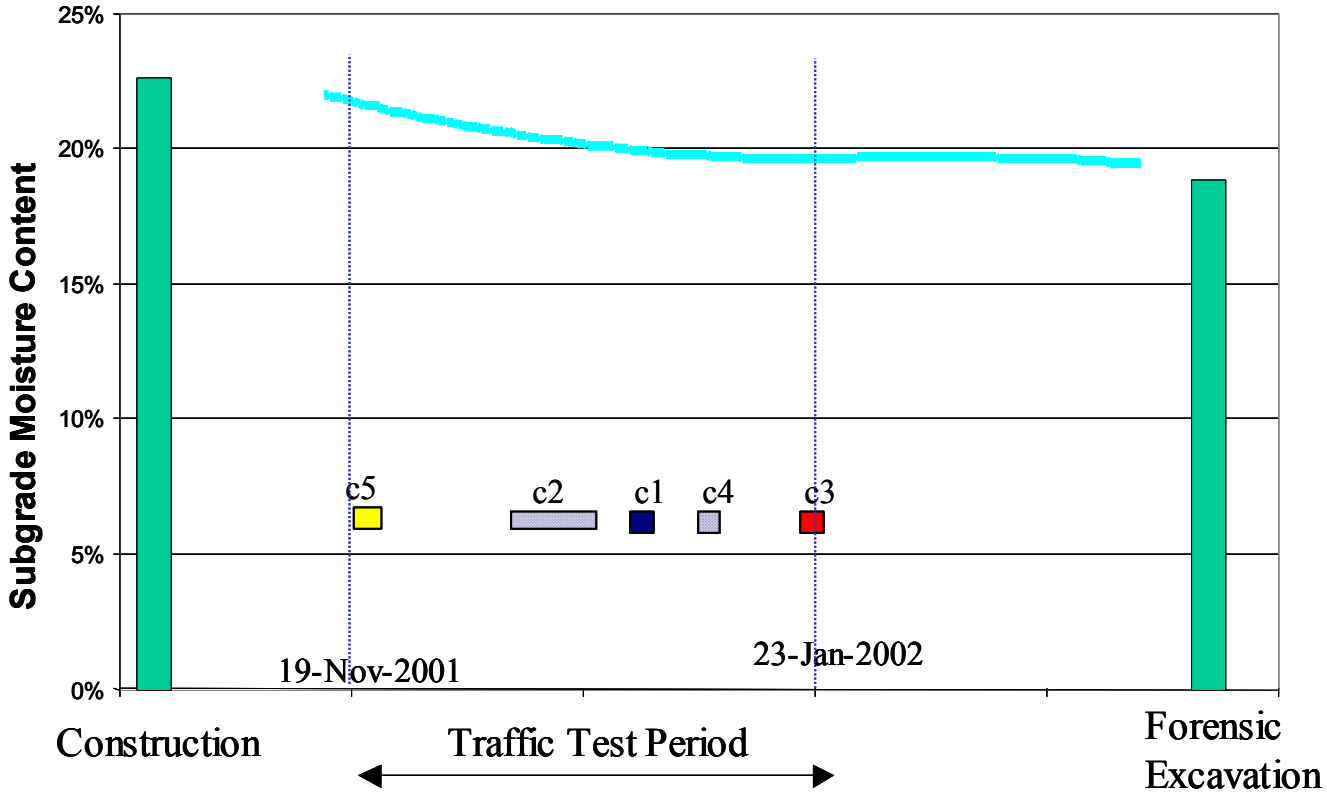

Figure 29. Moisture regime at the upper region of the subgrade.

Surface Rut Measurements

Transverse surface profile measurements were taken periodically during testing. The rut depth was calculated as the difference between the profile measurements taken at the pass level and the profile measurements taken prior to traffic testing. Profile measurements were taken every 30.5-cm starting at 15 cm from one end of the effective test window for a total of 20 locations. The acceleration and deceleration zones were excluded. An example of the surface profile data is presented in Figure 30. In this figure, positive values indicate compression.

The maximum rut depths from transverse profile measurements were used to develop the longitudinal profile. The longitudinal rut depth in various test windows as a function of load repetitions are presented in Figures 31 to 33. The ruts developed in this test section were quite irregular. Very large deformations occurred quickly upon application of traffic loads.

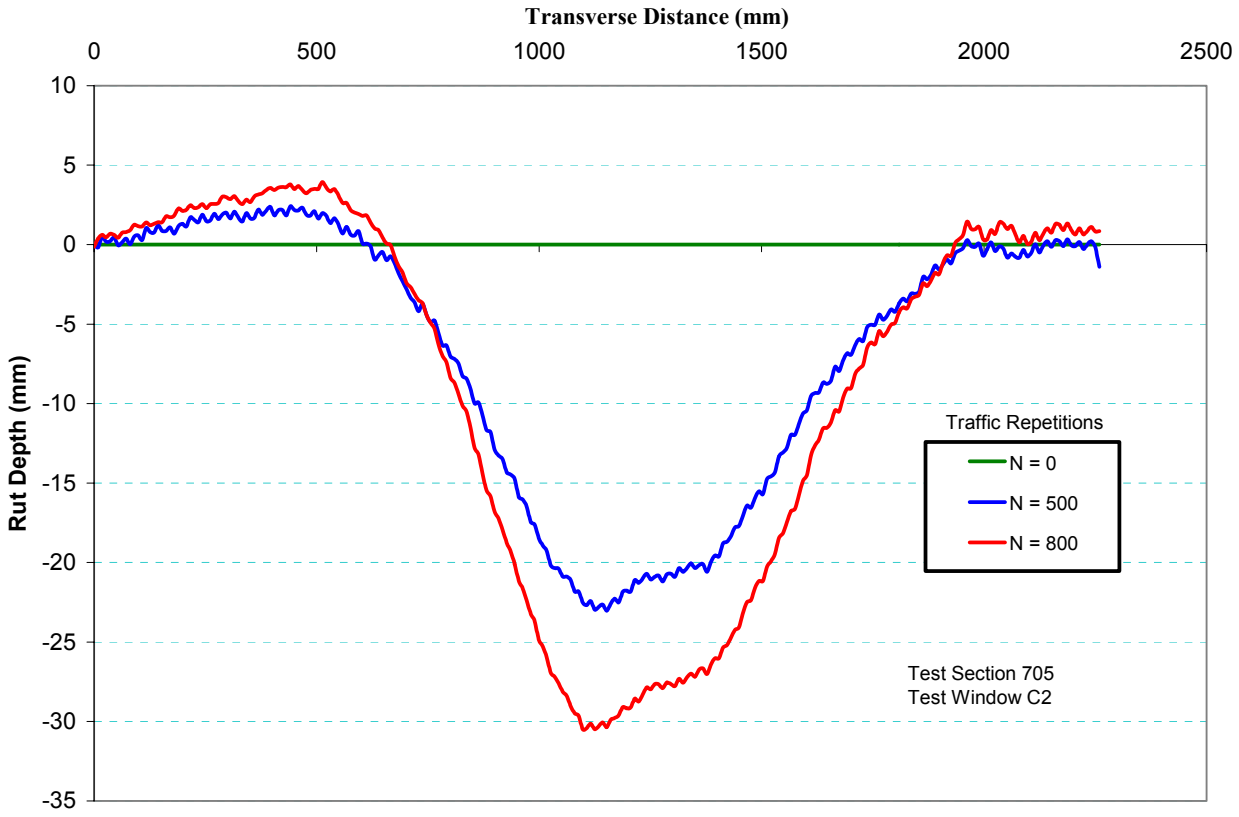

Figure 30. Typical transverse rut measurements in test section.

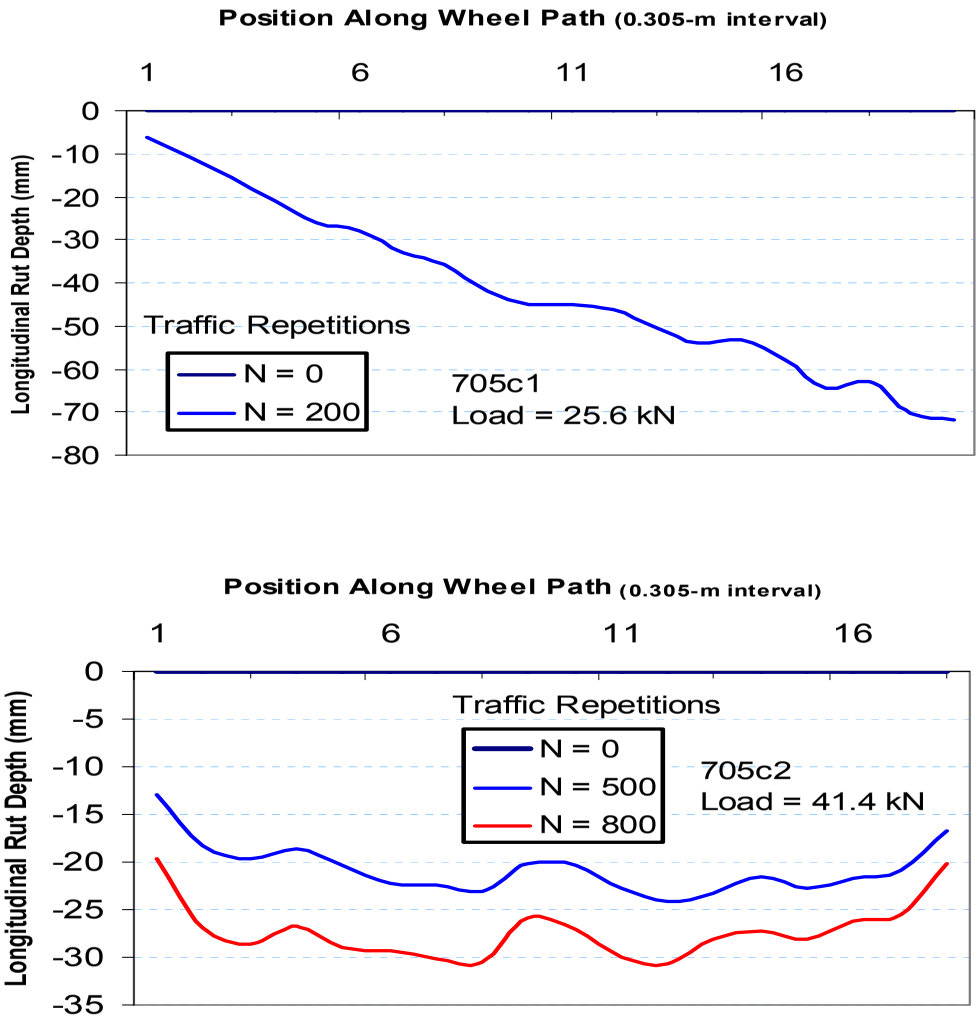

Figure 31. Longitudinal rut formation in TS705C1 and TS705C2

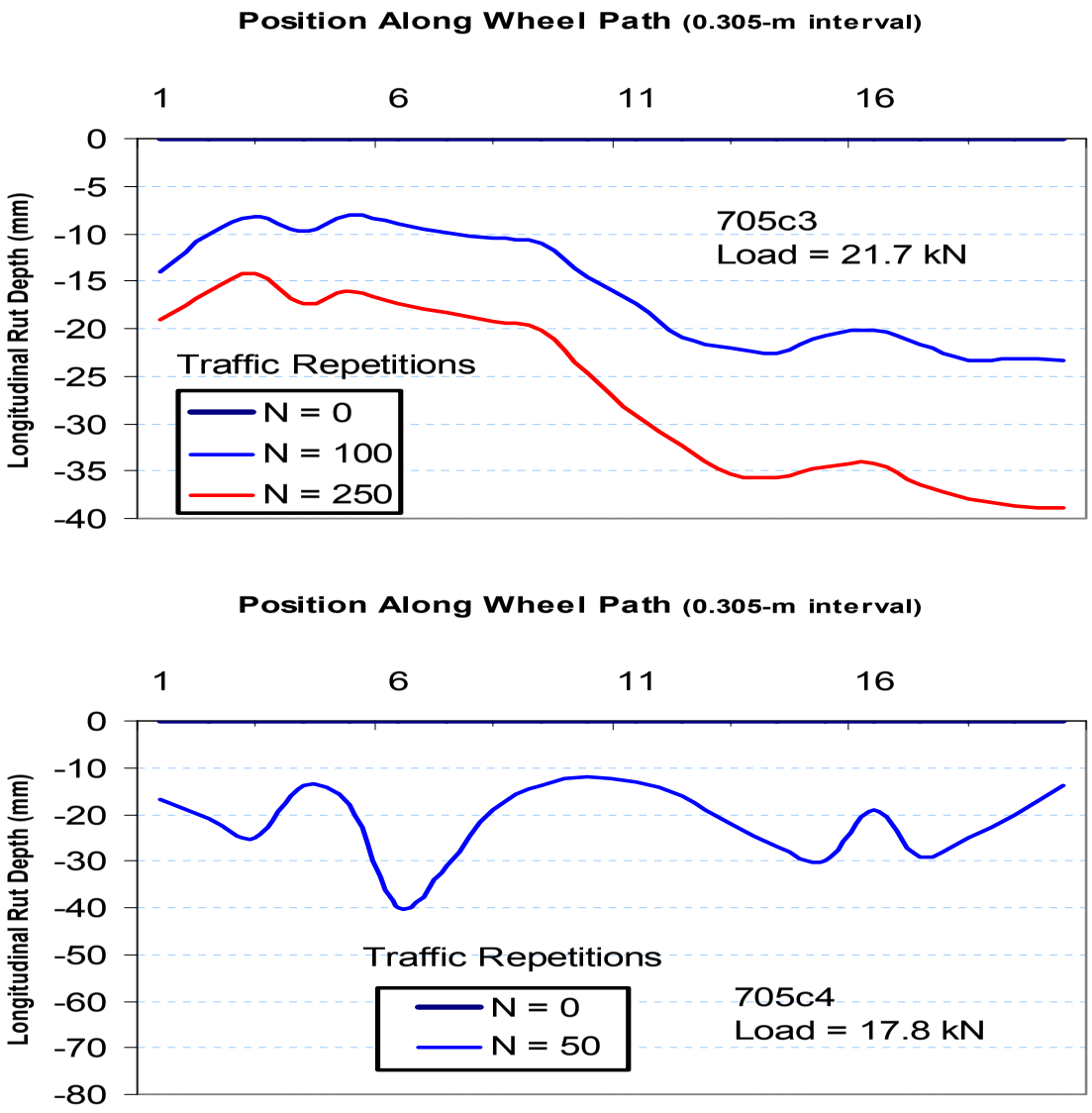

Figure 32. Longitudinal rut formation in TS705C3 and TS705C4.

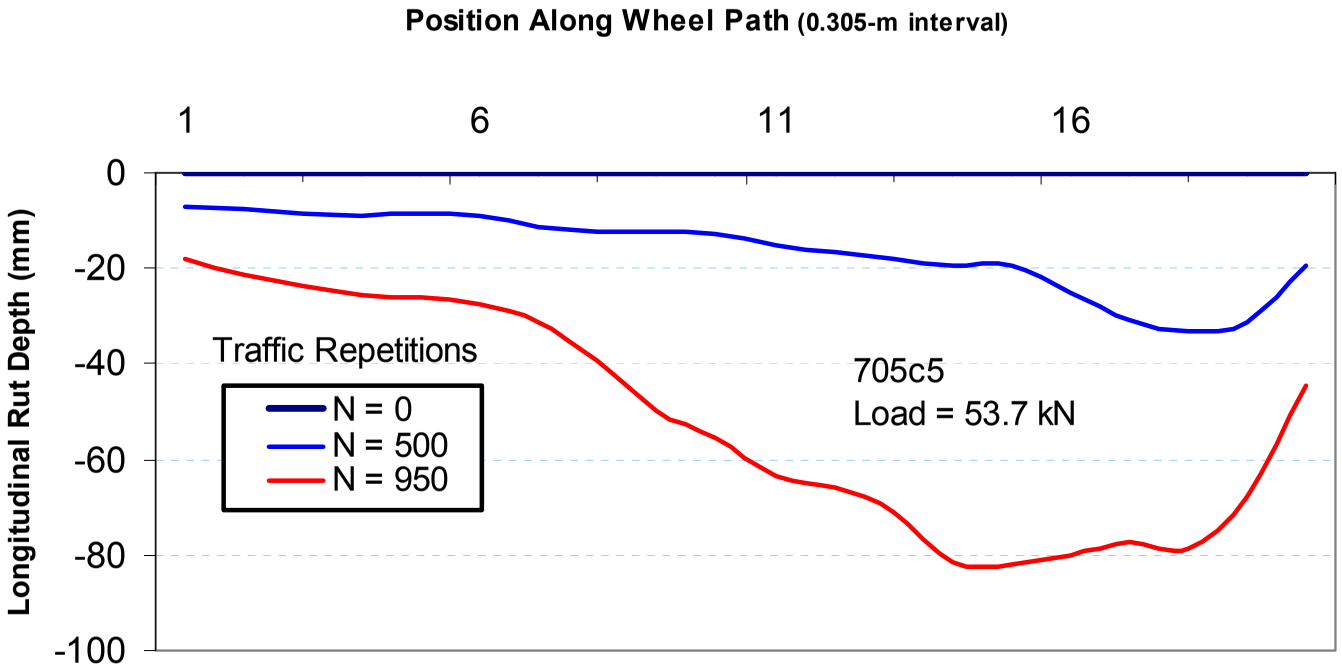

Figure 33. Longitudinal rut formation in TS704C5.

It was noticed that the HVS supports were sinking slowly but steadily even after placing plywood boards under the supports to spread the load.

A malfunction of the hydraulic system of the HVS resulted in a spill of hydraulic oil over the area of Test Window 705c4. An attempt was made to remove the spilled oil, but the asphalt concrete absorbed some oil. This type of oil dissolves petroleum products such as asphalt. Despite using a small load of only 17.8 kN, the pavement in Test Window c4 deflected dramatically under the test tires. The test was stopped at pass level 50 because the deformations were obviously beyond failure. The asphalt concrete was severely cracked.

Strain Measurements

Permanent and dynamic strain measurements were collected in the base course and at various depths in the subgrade. Unfortunately, the rut depths became excessive after only a small number of traffic passes even with loads as small as 17.8 kN.

Two separate stacks of emu coils were installed to enhance reliability. Stack A is the main stack, and it contains more coils. Stack B is the secondary stack that was set up as replicates the uppermost four vertical coil pairs and their coplanar companions. Stacks A and B are located near transverse rut measurement position 16 and position 8 respectively. However, we found, that the deformation patterns were significantly different at the two positions. We did not see differences of this magnitude in previous test sections and surmise that it may be unique to the very weak subgrade.

Dynamic Strain Measurements

Dynamic strain measurements are the transient strains developed as the tire assembly passes over the location where the sensors are embedded in the pavement. Static strain measurements are those strains that remain permanent well after the tire assembly has passed the location of the displacement sensors.

Dynamic strain measurements were obtained using εmu coil pairs. A proximity switch dictated the start of signal recording. A relay table managed by software developed in-house determined the order of coil measurements. With proper timing, every coil pair signal experiences a peak during dynamic loading. Tables 5 though 15 display the peak displacement for coil pairs in three orientations: vertical, longitudinal and transversal. The shape of the typical vertical and the longitudinal dynamic strain curves are simple and contain only one peak. Figure 34 shows the shape of a typical dynamic strain curve. It has three peaks. Each peak has been numbered, and this convention has been used consistently throughout this report.

Two separate stacks of emu coils were installed to enhance reliability. Stack A is the main stack, and it contains more coils. Stack B is the secondary stack that replicates the uppermost four vertical coil pairs and their coplanar companions.

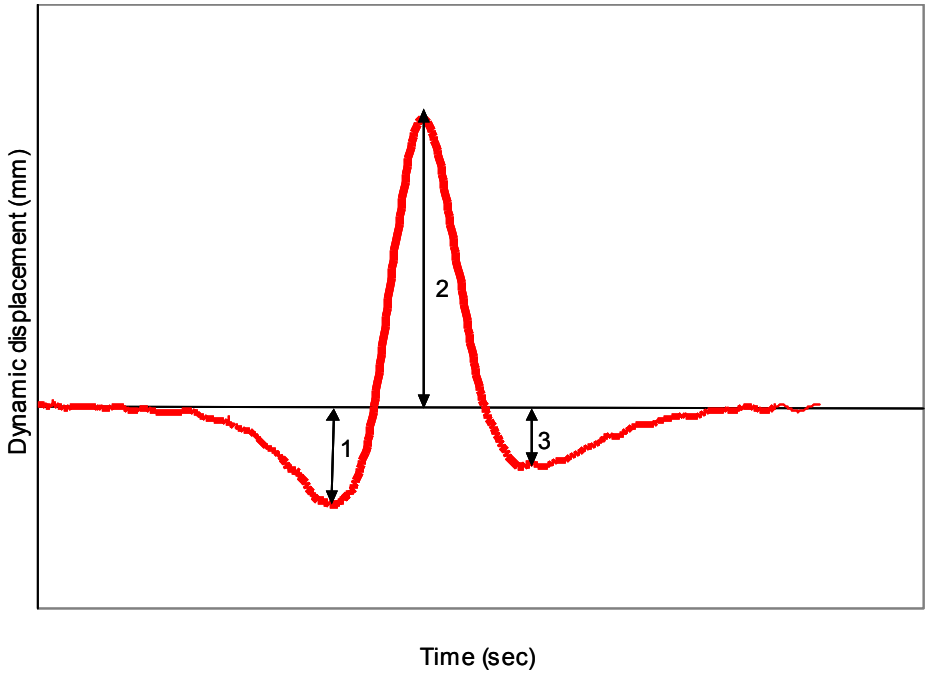

Figure 34. Components of a typical longitudinal dynamic displacement event.

Table 10a. Peak vertical displacement in Test Window 1, εmu Stack A.

	Peak Vertical Displacement (mm)	
	Pass Level	
Depth (mm)	0	200
133	-0.037	-0.059
248	-0.120	-0.076
381	-0.634	-1.428
533	-0.694	-1.581
686	-0.994	-1.203
838	-0.746	-0.816
991	-1.259	-2.309
1143	-0.472	-2.224
1295	-0.136	-0.462
1448	-0.075	-0.104

Table 10b. Peak vertical displacement in Test Window 1, Stack B.

	Peak Vertical Displacement (mm)	
	Pass Level	
Depth (mm)	0	200
133	-0.023	-0.221
248	-0.097	-0.160
381	-1.435	-1.216
533	-1.086	-0.940

Table 10c. Peak longitudinal displacement 1 in Test Window 1, Stack A.

	Peak Longitudinal Displacement (mm)	
	Pass Level	
Depth (mm)	0	200
76	-0.072	-0.050
191	-0.052	-0.097
305	-0.081	-0.296
457	-0.081	-0.370
610	-0.176	-0.326
762	-0.137	-0.245
914	-0.166	-0.311

Table 10d. Peak longitudinal displacement 1 in Test Window 1, Stack B.

	Peak Longitudinal Displacement (mm)	
	Pass Level	
Depth (mm)	0	200
76	-0.015	-0.034
191	-0.008	-0.007
305	-0.005	-0.006
457	-0.007	-0.017
610	-0.007	-0.010

Table 10e. Peak longitudinal displacement 2 in Test Window 1, Stack A.

	Peak Longitudinal Displacement (mm)	
	Pass Level	
Depth (mm)	0	200
76	0.322	0.356
191	0.178	0.313
305	0.249	0.685
457	0.242	0.701
610	0.479	0.860
762	0.424	0.671
914	0.343	0.518

Table 10f. Peak longitudinal displacement 2 in Test Window 1, Stack B.

	Peak Longitudinal Displacement (mm)	
	Pass Level	
Depth (mm)	0	200
76	0.377	0.227
191	0.276	0.366
305	0.505	0.581
457	0.584	0.660
610	0.486	0.572

Table 10g. Peak longitudinal displacement 3 in Test Window 1, Stack A.

	Peak Longitudinal Displacement (mm)	
	Pass Level	
Depth (mm)	0	200
76	-0.012	-0.081
191	-0.022	-0.086
305	-0.653	-0.100
457	-0.061	-0.108
610	-0.116	-0.108
762	-0.075	-0.114
914	-0.081	-0.120

Table 10h. Peak longitudinal displacement 3 in Test Window 1, Stack B.

	Peak Longitudinal Displacement (mm)	
	Pass Level	
Depth (mm)	0	200
76	-0.094	-0.136
191	-0.036	-0.101
305	-0.183	-0.236
457	-0.098	-0.203
610	-0.093	-0.170

Table 10i. Peak transverse displacement in Test Window 1, Stack A.

	Peak Transverse Displacement (mm)	
	Pass Level	
Depth (mm)	0	200
76	0.256	0.168
191	0.128	0.149
305	N/A	17.561
457	0.443	1.154
610	0.652	0.389
762	0.327	0.288
914	0.171	0.241

Table 10j. Peak transverse displacement in Test Window 1, Stack B.

	Peak Transverse Displacement (mm)	
	Pass Level	
Depth (mm)	0	200
76	0.020	0.012
191	0.029	0.028
305	0.035	0.013
457	0.065	0.015
610	0.081	0.048

Table 11a. Peak vertical displacement in Test Window 2, Stack A.

	Peak Vertical Displacement (mm)		
	Pass Level		
Depth (mm)	0	500	800
133	-0.151	-0.159	-0.178
248	-0.099	-0.071	-0.105
381	-0.539	-0.729	-0.728
533	-1.001	-1.453	-1.675
686	-1.199	-1.441	-1.422
838	-1.433	-1.672	-1.867
991	-0.910	-1.170	-1.224
1143	-1.306	-1.756	-1.872
1295	-0.803	-1.301	-1.498
1448	-0.110	-0.155	-0.154

Table 11b. Peak vertical displacement in Test Window 2, Stack B.

	Peak Vertical Displacement (mm)		
	Pass Level		
Depth (mm)	0	500	800
133	-0.359	-0.342	-0.477
248	-0.140	-0.148	-0.161
381	-1.115	-1.328	-1.470
533	-0.768	-0.905	-0.937

Table 11c. Peak longitudinal displacement 1 in Test Window 2, Stack A.

	Peak Longitudinal Displacement (mm)		
	Pass Level		
Depth (mm)	0	500	800
133	0.310	0.385	0.478
248	0.294	0.384	0.461
381	0.350	0.444	0.524
533	0.342	0.496	0.594
686	0.631	0.862	0.922
838	0.625	0.890	1.024
991	0.266	0.361	0.417

Table 11d. Peak longitudinal displacement 1 in Test Window 2, Stack B.

	Peak Longitudinal Displacement (mm)		
	Pass Level		
Depth (mm)	0	500	800
133	-0.005	-0.004	-0.006
248	-0.006	-0.005	-0.008
381	-0.007	-0.008	-0.013
533	-0.004	-0.005	-0.014
686	-0.030	-0.093	-0.088

Table 11e. Peak longitudinal displacement 2 in Test Window 2, Stack A.

	Peak Longitudinal Displacement (mm)		
	Pass Level		
Depth (mm)	0	500	800
133	-0.052	-0.054	-0.062
248	-0.096	-0.096	-0.103
381	-0.127	-0.145	-0.129
533	-0.176	-0.186	-0.172
686	-0.241	-0.192	-0.222
838	-0.252	-0.275	-0.284
991	-0.125	-0.146	-0.155

Table 11f. Peak longitudinal displacement 2 in Test Window 2, Stack B.

	Peak Longitudinal Displacement (mm)		
	Pass Level		
Depth (mm)	0	500	800
133	0.237	0.393	0.704
248	0.455	0.562	0.792
381	0.329	0.490	0.844
533	0.413	0.638	0.761
686	0.395	0.504	0.597

Table 11g. Peak longitudinal displacement 3 in Test Window 2, Stack A.

	Peak Longitudinal Displacement (mm)		
	Pass Level		
Depth (mm)	0	500	800
133	-0.052	-0.054	-0.062
248	-0.096	-0.096	-0.103
381	-0.127	-0.145	-0.129
533	-0.176	-0.186	-0.172
686	-0.241	-0.192	-0.222
838	-0.252	-0.275	-0.284
991	-0.125	-0.146	-0.155

Table 11h. Peak longitudinal displacement 3 in Test Window 2, Stack B.

	Peak Longitudinal Displacement (mm)		
	Pass Level		
Depth (mm)	0	500	800
133	-0.005	-0.004	-0.005
248	-0.005	-0.005	-0.009
381	-0.007	-0.009	-0.012
533	-0.004	-0.007	-0.012
686	-0.031	-0.089	-0.096

Table 11i. Peak transversal displacement in Test Window 2, Stack A.

	Peak Transversal Displacement (mm)		
	Pass Level		
Depth (mm)	0	500	800
133	0.281	0.156	0.165
248	0.314	0.229	0.232
381	0.407	0.462	0.406
533	0.603	0.870	0.960
686	0.589	0.625	0.644
838	0.465	0.497	0.553
991	0.271	0.380	0.383

Table 11j. Peak transversal displacement in Test Window 2, Stack B.

	Peak Transversal Displacement (mm)		
	Pass Level		
Depth (mm)	0	500	800
133	0.012	0.009	0.006
248	0.031	0.007	0.015
381	0.023	0.006	0.009
533	0.060	0.013	0.008
686	0.072	0.060	0.063

Table 12a. Peak vertical displacement 3 in Test Window 3, Stack A.

	Peak Vertical Displacement (mm)		
	Pass Level		
Depth (mm)	0	100	250
133	-0.254	-0.046	-0.326
248	-0.085	-0.058	-0.137
381	-0.607	-0.904	-1.128
533	-0.842	-1.230	-1.401
686	-0.762	-1.020	-1.189
838	-0.721	-0.976	-1.176
991	-0.576	-0.810	-1.137
1143	-0.438	-0.708	-1.040
1295	-0.208	-0.492	-0.557
1448	-0.051	-0.076	-0.111

Table 12b. Peak vertical displacement 3 in Test Window 3, Stack B.

	Peak Vertical Displacement (mm)		
	Pass Level		
Depth (mm)	0	100	250
133	-0.049	-0.057	-0.047
248	-0.056	-0.054	-0.082
381	-0.565	-0.762	-0.857
533	-0.455	-0.750	-0.753

Table 12c. Peak longitudinal Displacement 1 in Test Window 3, Stack A.

	Peak Longitudinal Displacement (mm)		
	Pass Level		
Depth (mm)	0	100	250
133	-0.025	-0.038	-0.041
248	-0.031	-0.047	-0.063
381	-0.076	-0.118	-0.165
533	-0.160	-0.222	-0.271
686	-0.153	-0.205	-0.239
838	-0.108	-0.168	-0.199
991	-0.121	-0.196	-0.242

Table 12d. Peak longitudinal displacement 1 in Test Window 3, Stack B.

	Peak Longitudinal Displacement (mm)		
	Pass Level		
Depth (mm)	0	100	250
133	-0.006	-0.006	-0.006
248	-0.005	-0.005	-0.006
381	-0.003	-0.004	-0.004
533	-0.007	-0.004	-0.026
686	-0.005	-0.008	-0.032

Table 12e. Peak longitudinal displacement 2 in Test Window 3, Stack A.

	Peak Longitudinal Displacement (mm)		
	Pass Level		
Depth (mm)	0	100	250
133	-0.061	-0.053	-0.052
248	-0.031	-0.030	-0.024
381	-0.047	-0.069	-0.063
533	-0.052	-0.099	-0.138
686	-0.066	-0.105	-0.131
838	-0.066	-0.083	-0.130
991	-0.050	-0.066	-0.114

Table 12f. Peak longitudinal displacement 2 in Test Window 3, Stack B.

	Peak Longitudinal Displacement (mm)		
	Pass Level		
Depth (mm)	0	100	250
133	-0.057	-0.082	-0.073
248	-0.029	-0.049	-0.065
381	-0.071	-0.116	-0.137
533	-0.097	-0.154	-0.188
686	-0.062	-0.113	-0.163

Table 12g. Peak longitudinal displacement 3 in Test Window 3, Stack A.

	Peak Longitudinal Displacement (mm)		
	Pass Level		
Depth (mm)	0	100	250
133	-0.061	-0.053	-0.052
248	-0.031	-0.030	-0.024
381	-0.047	-0.069	-0.063
533	-0.052	-0.099	-0.138
686	-0.066	-0.105	-0.131
838	-0.066	-0.083	-0.130
991	-0.050	-0.066	-0.114

Table 12h. Peak longitudinal displacement 3 in Test Window 3, Stack B.

	Peak Longitudinal Displacement (mm)		
	Pass Level		
Depth (mm)	0	100	250
133	-0.057	-0.082	-0.073
248	-0.029	-0.049	-0.065
381	-0.071	-0.116	-0.137
533	-0.097	-0.154	-0.188
686	-0.062	-0.113	-0.163

Table 12i. Peak transversal displacement 3 in Test Window 3, Stack A.

	Peak Transversal Displacement (mm)		
	Pass Level		
Depth (mm)	0	100	250
133	0.232	0.239	0.236
248	0.143	0.174	0.101
381	0.155	0.293	0.284
533	0.429	0.655	0.575
686	0.427	0.400	0.384
838	0.364	0.438	0.556
991	0.334	0.441	0.483

Table 12j. Peak transversal displacement 3 in Test Window 3, Stack B.

	Peak Transversal Displacement (mm)		
	Pass Level		
Depth (mm)	0	100	250
133	0.005	0.009	0.009
248	0.008	0.008	0.011
381	0.005	0.008	0.003
533	0.008	0.021	0.011
686	0.022	0.047	0.028

Table 13a. Peak vertical displacement in Test Window 4, Stack A.

	Peak Vertical Displacement (mm)
	Pass Level
Depth (mm)	0
133	-21.242
248	-0.084
381	-1.206
533	-3.082
686	-2.223
838	-0.739
991	-2.608
1143	-2.297
1295	-0.771
1448	-0.156

Table 13b. Peak vertical displacement in Test Window 4, Stack B.

	Peak Vertical Displacement (mm)
	Pass Level
Depth (mm)	0
133	-27.928
248	-0.456
381	-0.546
533	-0.718

Table 13c. Peak longitudinal displacement 1 in Test Window 4, Stack A.

	Peak Vertical Displacement (mm)
	Pass Level
Depth (mm)	0
133	-0.134
248	-0.187
381	-0.319
533	-0.797
686	-0.802
838	-0.663
991	-0.717

Table 13d. Peak longitudinal displacement 1 in Test Window 4, Stack B.

	Peak Vertical Displacement (mm)
	Pass Level
Depth (mm)	0
133	-0.009
248	-0.022
381	-0.003
533	-0.009

Table 13e. Peak longitudinal displacement 2 in Test Window 4, Stack A.

	Peak Longitudinal Displacement (mm)
	Pass Level
Depth (mm)	0
133	0.135
248	0.236
381	0.382
533	0.741
686	0.715
838	0.890
991	0.793

Table 13f. Peak longitudinal displacement 2 in Test Window 4, Stack B.

	Peak Longitudinal Displacement (mm)
	Pass Level
Depth (mm)	0
133	0.163
248	0.141
381	0.202
533	0.305

Table 13f. Peak longitudinal displacement 3 in Test Window 4, Stack A.

	Peak Longitudinal Displacement (mm)
	Pass Level
Depth (mm)	0
133	-0.309
248	-0.107
381	-0.178
533	-0.270
686	-0.001
838	-0.096
991	-0.121

Table 13g. Peak longitudinal displacement 3 in Test Window 4, Stack B.

	Peak Longitudinal Displacement (mm)
	Pass Level
Depth (mm)	0
133	-0.066
248	-0.477
381	-0.108
533	-0.153

Table 13h. Peak transversal in Test Window 4, Stack A.

	Peak Transverse Displacement (mm)
	Pass Level
Depth (mm)	0
133	1.630
248	0.218
381	0.663
533	0.719
686	0.935
838	0.794
991	0.593

Table 13g. Peak transversal Stack B

	Peak Transverse Displacement (mm)
	Pass Level
Depth (mm)	0
133	0.0200
248	0.0863
381	0.0088
533	0.0181

Table 14a. Peak vertical displacement in Test Window 5, Stack A.

	Peak Vertical Displacement (mm)		
	Pass Level		
Depth (mm)	0	500	950
133	-0.076	-0.163	-0.714
248	-0.076	-0.149	-0.279
381	-0.297	-0.771	-1.631
533	-1.107	-1.413	-3.501
686	-0.489	-1.227	-2.489
838	-0.249	-0.672	-0.915
991	-0.337	-1.061	-2.007
1143	-1.385	-3.841	-5.852
1295	-0.161	-0.741	-1.110
1448	-0.069	-0.246	-0.534

Table 14b. Peak vertical displacement in Test Window 5, Stack B.

	Peak Vertical Displacement (mm)		
	Pass Level		
Depth (mm)	0	500	950
133	-0.205	-0.493	-0.720
248	-0.204	-0.487	-0.696
381	-0.202	-0.501	-0.705
533	-0.358	-0.551	-0.959

Table 14c. Peak longitudinal displacement 1 in Test Window 5, Stack A.

	Peak Longitudinal Displacement (mm)		
	Pass Level		
Depth (mm)	0	500	950
133	-0.033	-0.048	-3.129
248	-0.029	-0.041	-0.180
381	-0.036	-0.055	-0.111
533	-24.615	-24.450	-33.743
686	-0.454	-0.949	-1.664
838	-0.086	-0.090	-0.283
991	-0.120	-0.175	-0.665

Table 14d. Peak longitudinal displacement 1 in Test Window 5, Stack B.

	Peak Longitudinal Displacement (mm)		
	Pass Level		
Depth (mm)	0	500	950
133	-0.061	-0.061	-0.209
248	-0.057	-0.068	-0.279
381	-0.068	-0.078	-0.145
533	-0.077	-0.078	-0.194

Table 14e. Peak longitudinal displacement 2 in Test Window 5, Stack A.

	Peak Longitudinal Displacement (mm)		
	Pass Level		
Depth (mm)	0	500	950
133	0.110	0.131	4.816
248	0.076	0.159	4.818
381	0.131	0.265	0.627
533	50.543	50.317	42.274
686	0.078	0.061	0.099
838	0.212	0.418	1.412
991	0.067	0.118	0.738

Table 14f. Peak longitudinal displacement 2 in Test Window 5, Stack B.

	Peak Longitudinal Displacement (mm)		
	Pass Level		
Depth (mm)	0	500	950
133	0.072	0.076	0.934
248	0.076	0.085	0.700
381	0.044	0.095	0.139
533	0.069	0.081	2.758

Table 14g. Peak longitudinal displacement 3 in Test Window 5, Stack A.

	Peak Longitudinal Displacement (mm)		
	Pass Level		
Depth (mm)	0	500	950
133	-0.019	-0.002	-3.066
248	-0.002	0.000	-0.002
381	-0.017	-0.011	-0.018
533	-0.786	-15.751	-9.123
686	-0.121	-0.248	-0.180
838	-0.114	-0.086	-0.257
991	-0.089	-0.091	-0.174

Table 14h. Peak longitudinal displacement 3 in Test Window 5, Stack B.

	Peak Longitudinal Displacement (mm)		
	Pass Level		
Depth (mm)	0	500	950
133	-0.063	-0.087	-0.893
248	-0.064	-0.070	-0.585
381	-0.070	-0.109	-0.076
533	-0.122	-0.168	-1.874

Table 14i. Peak transversal displacement in Test Window 5, Stack A.

	Peak Transversal Displacement (mm)		
	Pass Level		
Depth (mm)	0	500	950
133	0.001	0.001	0.001
248	0.001	0.002	0.002
381	0.002	0.004	0.004
533	0.004	0.004	0.004
686	0.001	0.002	0.002
838	0.078	0.080	0.088
991	0.203	0.219	0.297

Table 14j. Peak transversal displacement in Test Window 5, Stack B.

	Peak Transversal Displacement (mm)		
	Pass Level		
Depth (mm)	0	500	950
133	0.080	0.101	0.101
248	0.096	0.106	0.097
381	0.008	0.010	0.008
533	0.007	0.007	0.007

Permanent Strain Measurements

The measured permanent deformations and strains are presented in Tables 6 and 7. Note no measurements were made in C4 and C6. There was a mechanical failure of the HVS, resulting in hydraulic oil spillage on to the test window C4. The section rutted severely within 50 passes. By the time it came to testing window C6, the test section was severely deformed that conducting any tests on window C6 was considered meaningless.

Table 15a. Average permanent deformation in 705C1.

STACK A 705C1								
Vertical Deformation (mm)			Longitudinal Deformation (mm)			Transverse Deformation (mm)		
	Load Repetition			Load Repetition			Load Repetition	
Depth (mm)	0	200	Depth (mm)	0	200	Depth (mm)	0	200
Surface	0	-1.2000						
133	0	-4.2776	76	0	1.0241	76	0	2.9906
248	0	-1.7823	191	0	-0.5159	191	0	1.1943
381	0	-4.0073	305	0	-0.2969	305	0	50.4405
533	0	-2.3300	457	0	-0.2926	457	0	4.4770
686	0	-4.2936	610	0	0.5015	610	0	0.9720
838	0	-2.5975	762	0	0.5208	762	0	3.1369
991	0	-4.7144	914	0	-0.3679	914	0	2.1773
1143	0	-2.2401						
1295	0	0.0940						
1448	0	0.0005						

STACK B 705C1								
Vertical Deformation (mm)			Longitudinal Deformation (mm)			Transverse Deformation (mm)		
	Load Repetition			Load Repetition			Load Repetition	
Depth (mm)	0	200	Depth (mm)	0	200	Depth (mm)	0	200
Surface	0							
133	0	-0.1636	76	0	-0.0759	76	0	0.4592
248	0	-1.4329	191	0	-0.0097	191	0	0.8552
381	0	-2.7368	305	0	0.3817	305	0	1.4555
533	0	-1.0816	457	0	0.2498	457	0	1.9043

Table 15b. Average permanent deformation in 705C2.

STACK A 705C2										
Vertical Deformation (mm)				Longitudinal Deformation (mm)				Transverse Deformation (mm)			
	Load Repetition				Load Repetition				Load Repetition		
Depth (mm)	0	500	800	Depth (mm)	0	500	800	Depth (mm)	0	500	800
Surface	0	-2.6000	-3.2000								
133	0	-2.9208	-3.7109	76	0	0.1286	0.0913	76	0	1.4801	1.6018
248	0	-1.7392	-2.1807	191	0	-0.4396	-0.6714	191	0	1.3046	1.5131
381	0	-1.6073	-2.1079	305	0	-0.2910	-0.2837	305	0	1.1038	1.3147
533	0	-2.4418	-3.0513	457	0	-0.3843	-0.5488	457	0	2.3549	3.2167
686	0	-1.6545	-2.3967	610	0	-0.5730	-0.3668	610	0	0.7259	0.9366
1219	0	-2.5919	-3.2564	762	0	0.3183	0.3766	762	0	1.6864	2.2176
1448	0	-1.4738	-1.9130	914	0	-0.1075	-0.1536	914	0	1.2922	1.6774
1676	0	-2.4208	-3.0102								
1905	0	0.2926	0.5936								
2134	0	0.0060	-0.0091								

STACK B 705C2										
Vertical Deformation (mm)				Longitudinal Deformation (mm)				Transverse Deformation (mm)			
	Load Repetition				Load Repetition				Load Repetition		
Depth (mm)	0	500	800	Depth (mm)	0	500	800	Depth (mm)	0	500	800
Surface	0										
133	0	-5.6699	-8.2216	76	0	0.0616	-0.1620	76	0	1.5022	2.3518
248	0	-2.3093	-3.3299	191	0	0.0723	0.3760	191	0	1.1965	1.6889
381	0	-4.1229	-6.0885	305	0	-0.3555	-0.5434	305	0	0.7575	1.0157
533	0	-1.5219	-2.3350	457	0	0.2616	0.4276	457	0	1.3714	2.0733
				610	0	0.2508	0.3738	610	0	1.2589	1.8437

Table 15c. Average permanent deformation in 705C3.

STACK A 705C3											
Vertical Deformation (mm)				Longitudinal Deformation (mm)				Transverse Deformation (mm)			
	Load Repetition				Load Repetition				Load Repetition		
Depth (mm)	0	100	250	Depth (mm)	0	100	250	Depth (mm)	0	100	250
Surface	0	-1.2000	-1.7000								
133	0	-1.0909	-1.9227	76	0	-0.1303	-0.2309	76	0	1.4348	2.3150
248	0	-0.6866	-1.6652	191	0	-0.2228	-0.3201	191	0	1.0389	1.3990
381	0	-1.9355	-4.0279	305	0	-0.2552	-0.5382	305	0	0.9466	1.5710
533	0	-2.0293	-3.9424	457	0	-0.0103	0.1034	457	0	2.0181	3.7945
686	0	-1.7795	-3.2072	610	0	-0.0940	-0.2262	610	0	1.3235	2.1371
1219	0	-1.3372	-3.1985	762	0	-0.2663	-0.4910	762	0	1.4364	2.7941
1448	0	-0.9598	-2.4812	914	0	-0.1606	-0.3153	914	0	1.1381	2.1604
1676	0	-0.7110	-1.7792								
1905	0	-0.3673	-1.0349								
2134	0	-0.0070	0.0245								

STACK B 705C3											
Vertical Deformation (mm)				Longitudinal Deformation (mm)				Transverse Deformation (mm)			
	Load Repetition				Load Repetition				Load Repetition		
Depth (mm)	0	100	250	Depth (mm)	0	100	250	Depth (mm)	0	100	250
Surface	0										
133	0	-0.3372	-0.8090	76	0	-0.0130	-0.1073	76	0	0.9333	1.6532
248	0	-0.2919	-0.8327	191	0	-0.1100	-0.2469	191	0	0.7223	1.2520
381	0	-1.0908	-2.5053	305	0	-0.0414	-0.0801	305	0	0.6193	1.2376
533	0	-0.8466	-1.9107	457	0	0.1002	0.2365	457	0	0.8933	1.7004
				610	0	-0.1572	-0.2570	610	0	0.9972	1.7609

Table 16a. Average permanent strain in 705C1.

STACK A 705C1								
Vertical Strain (mm)			Longitudinal Strain (mm)			Transverse Strain (mm)		
	Load Repetition			Load Repetition			Load Repetition	
Depth (mm)	0	200	Depth (mm)	0	200	Depth (mm)	0	200
Surface	0	-1.579						
133	0	-4.041	76	0	0.611	76	0	2.137
248	0	-1.681	191	0	-0.378	191	0	1.032
381	0	-2.863	305	0	-0.208	305	0	8.257
533	0	-1.453	457	0	-0.210	457	0	3.784
686	0	-2.888	610	0	0.354	610	0	0.844
838	0	-1.866	762	0	0.390	762	0	2.722
991	0	-2.379	914	0	-0.250	914	0	1.536
1143	0	-1.101						
1295	0	0.080						
1448	0	0.000						

STACK B 705C1								
Vertical Strain (mm)			Longitudinal Strain (mm)			Transverse Strain (mm)		
	Load Repetition			Load Repetition			Load Repetition	
Depth (mm)	0	200	Depth (mm)	0	200	Depth (mm)	0	200
Surface	0							
133	0	-0.130	76	0	-0.046	76	0	0.283
248	0	-1.201	191	0	-0.006	191	0	0.551
381	0	-1.793	305	0	0.239	305	0	0.923
533	0	-0.733	457	0	0.159	457	0	1.216

Table 16b. Average permanent strain in 705C2.

STACK A 705C2											
Vertical Strain (%)				Longitudinal Strain (%)				Transverse Strain (%)			
	Load Repetition				Load Repetition				Load Repetition		
Depth (mm)	0	500	800	Depth (mm)	0	500	800	Depth (mm)	0	500	800
Surface	0	-3.421	-4.211								
133	0	-2.435	-3.094	76	0	0.082	0.058	76	0	0.855	0.925
248	0	-1.484	-1.861	191	0	-0.249	-0.380	191	0	0.686	0.796
381	0	-1.117	-1.465	305	0	-0.186	-0.182	305	0	0.611	0.727
533	0	-1.758	-2.196	457	0	-0.227	-0.324	457	0	1.450	1.981
686	0	-1.045	-1.514	610	0	-0.330	-0.211	610	0	0.439	0.566
1219	0	-1.547	-1.944	762	0	0.199	0.235	762	0	1.006	1.323
1448	0	-1.004	-1.303	914	0	-0.074	-0.106	914	0	0.864	1.122
1676	0	-1.294	-1.609								
1905	0	0.298	0.605								
2134	0	0.005	-0.007								

STACK B 705C2											
Vertical Strain (%)				Longitudinal Strain (%)				Transverse Strain (%)			
	Load Repetition				Load Repetition				Load Repetition		
Depth (mm)	0	500	800	Depth (mm)	0	500	800	Depth (mm)	0	500	800
Surface	0										
133	0	-2.462	-3.571	76	0	0.041	-0.108	76	0	1.084	1.697
248	0	-1.874	-2.703	191	0	0.047	0.243	191	0	0.782	1.103
381	0	-1.541	-2.275	305	0	-0.218	-0.334	305	0	0.486	0.652
533	0	-1.173	-1.800	457	0	0.161	0.263	457	0	0.880	1.330
				610	0	0.151	0.225	610	0	0.797	1.168

Table 16c. Average permanent strain in 705C3.

STACK A 705C3										
Vertical Strain (%)				Longitudinal Strain (%)				Transverse Strain (%)			
	Load Repetition				Load Repetition				Load Repetition		
Depth (mm)	0	100	250	Depth (mm)	0	100	250	Depth (mm)	0	100	250
Surface	0	-1.579	-2.237								
133	0	-0.822	-1.448	76	0	-0.083	-0.146	76	0	0.905	1.460
248	0	-0.589	-1.428	191	0	-0.145	-0.208	191	0	0.659	0.888
381	0	-0.991	-2.063	305	0	-0.176	-0.371	305	0	0.598	0.993
533	0	-1.257	-2.443	457	0	-0.007	0.068	457	0	1.350	2.538
686	0	-1.149	-2.070	610	0	-0.063	-0.150	610	0	0.872	1.409
1219	0	-0.917	-2.194	762	0	-0.181	-0.334	762	0	0.951	1.851
1448	0	-0.607	-1.570	914	0	-0.107	-0.210	914	0	0.763	1.448
1676	0	-0.436	-1.090								
1905	0	-0.328	-0.924								
2134	0	-0.005	0.017								

STACK B 705C3										
Vertical Strain (%)				Longitudinal Strain (%)				Transverse Strain (%)			
	Load Repetition				Load Repetition				Load Repetition		
Depth (mm)	0	100	250	Depth (mm)	0	100	250	Depth (mm)	0	100	250
Surface	0										
133	0	-0.369	-0.885	76	0	-0.008	-0.069	76	0	0.665	1.178
248	0	-0.240	-0.685	191	0	-0.079	-0.177	191	0	0.504	0.874
381	0	-0.665	-1.527	305	0	-0.026	-0.051	305	0	0.433	0.865
533	0	-0.594	-1.341	457	0	0.068	0.160	457	0	0.615	1.172
				610	0	-0.108	-0.176	610	0	0.676	1.193

Table 16d. Average permanent strain in 705C5.

STACK A 705C5											
Vertical Strain (%)				Longitudinal Strain (%)				Transverse Strain (%)			
	Load Repetition				Load Repetition				Load Repetition		
Depth (mm)	0	500	950	Depth (mm)	0	500	950	Depth (mm)	0	500	950
Surface	0										
133	0	-1.654	-4.280	76	0	-0.228	-3.065	76	0	0.443	0.698
248	0	-0.984	-2.915	191	0	-3.212	-1.747	191	0	0.627	1.163
381	0	-0.612	-1.330	305	0	-0.213	-0.463	305	0	0.911	2.179
533	0	-2.370	-5.964	457	0	-0.121	3.988	457	0	1.451	5.214
686	0	-2.332	-5.421	610	0	-1.376	-2.357	610	0	1.982	5.949
1219	0	-1.730	-4.390	762	0	0.505	1.166	762	0	-0.432	-1.386
1448	0	-2.073	-4.677	914	0	0.264	0.755	914	0	0.771	3.413
1676	0	-2.815	-7.981								
1905	0	-1.166	-2.029								
2134	0	-0.178	-0.538								

STACK B 705C5											
Vertical Strain (%)				Longitudinal Strain (%)				Transverse Strain (%)			
	Load Repetition				Load Repetition				Load Repetition		
Depth (mm)	0	500	950	Depth (mm)	0	500	950	Depth (mm)	0	500	950
Surface	0										
133	0	-0.640	-1.530	76	0	-0.041	-0.454	76	0	-0.003	0.212
248	0	-0.634	-1.520	191	0	-0.083	-0.461	191	0	-0.010	0.168
381	0	-0.646	-1.536	305	0	0.096	-0.281	305	0	-0.297	-0.527
533	0	-0.875	-1.941	457	0	-0.138	-1.065	457	0	-0.274	-0.468
				610	0	-0.089	-0.685	610	0	-0.353	-1.123

Stress Measurements

Results from the stress measurements are presented in Table 17. Triaxial stress measurements were taken at a depth of 381 mm form the AC surface. In test windows 705C2 and 705C5, additional stress measurements were made at a depth of 533 mm.

We found the vertical stress measurements to be noisy and the peak values were considered to be low. In addition, they did not show significant difference as a function of depth. This suggests that under the load, the stress cells actually moved in the soft soil and did not register the actual pressures. No further analysis were carried with the stress data.

Table 17. Measured stresses in test windows.

Window	Load (kN)	Depth (mm)	Load Repetiton	Stress		
				Vertical	Longitudinal	Transverse
705C1	26	381	0	-5.53	3.03	-5.43
			200	-7.28	4.56	-7.06
705C2	41	381	0	-10.39	9.90	-4.25
			500	-11.96	8.38	-4.94
			800	-14.24	8.37	-5.33
		533	0	-12.17	7.98	-6.37
			500	-12.63	8.38	-6.79
			800	-13.60	8.12	-6.92
705C3	22	381	0	-12.47	4.92	-6.28
			100	-14.62	5.78	-8.10
			250	-19.07	8.21	-5.74
705C5	54	381	0	-14.86	9.67	-2.94
			500	-24.45	12.00	-6.39
			950	-29.92	12.49	-8.24
		533	0	-15.93		-5.80
			500	-21.17		-8.26
			950	-22.80		-9.06

Tire pressure = 690 kPa

8 FORENSIC EVALUATION

For each soil type, the research plan includes one test section at optimum moisture content and two test sections at other moisture contents. The research team designed the experiment in the current test section (Test Section 705) to represent a moisture condition near the extreme wet for this subgrade soil. Measuring the pavement response to traffic under these conditions would provide the means to interpolate test parameters between those at extreme moisture content and those at optimum moisture content. Interpolation is usually more reliable than extrapolation. Previous experiments suggest that for most fine-grained soils, the moisture content that yields a CBR of 1 is near the constructability limit, i.e. further moisture content renders the soil muddy and unstable. Therefore, the target gravimetric moisture content for the subgrade soil in Test Section 705 was 23 percent. Figure 6 indicates that the A-4 subgrade soil at 23 percent has a CBR value of 1. It is very difficult to build a pavement test section with a very soft soil because subsequent construction traffic can cause large surface ruts. After the subgrade was finished and the base course was carefully built, the paving equipment caused large ruts. The ruts were filled with asphalt concrete to produce a flat upper surface, but this resulted in significant asphalt thickness variations.

Upon setting of the HVS over the test area, the pavement surface deformed significantly despite the precaution of covering the area with plywood boards. The maximum pavement deformation occurred at the HVS supports despite placing several layers of wood to help spread the loads. The HVS supports continued to sink into the pavement slowly and gradually. The deformation appeared to be time-dependent. Rod and level measurements were conducted to monitor changes in elevation at various points in the test windows.

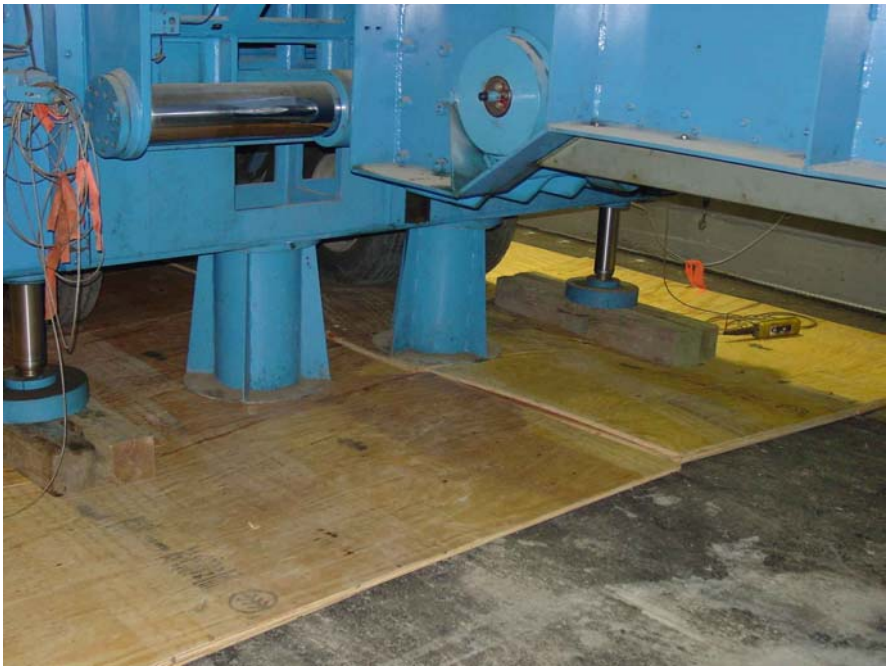

Figure 35. Pavement deformation at the HVS supports.

Only few traffic passes were required to cause rutting beyond failure. Both the resilient and the permanent deformations were large even with loads as light as 17.8 kN (4 kips). Figure 36 shows dramatic rutting and cracking at the end of 1000 passes with a load of 53.7 kN (12 kips).

Figure 36. Pavement rutting and cracking at the end of HVS traffic on Test Window 5.

A mechanical failure of the hydraulic system of the HVS caused an oil spill that further weakened the asphalt pavement in Test Window 4. For other test sections, there appears to be only insignificant interaction between test windows. In this test section, cracks and surface deformation from one test window extended into neighboring test windows. The damage induced onto Test Window 6 by the action of traffic on Test Window 5 was so dramatic that the research team decided not to test this window.

A forensic exploration was conducted to establish the condition of the pavement structure at the end of the traffic tests and to search for facts that could help understand the unusual pavement response to traffic.

One trench was excavated across test windows 1, 2, and 3 on the South region of the test section. Another trench was excavated in the north region of the test section. This trench cut across test windows 4, 5, and 6.

The trenches had to be carefully located to avoid damaging the embedded sensors.

The areas of the trenches were marked with paint over the asphalt pavement. A dry saw was used to neatly cut the asphalt pavement so that reliable layer thickness measurements could be made. Rod and level elevation measurements were taken at 0.20-m (8 in) spacing along the edge of the trenches.

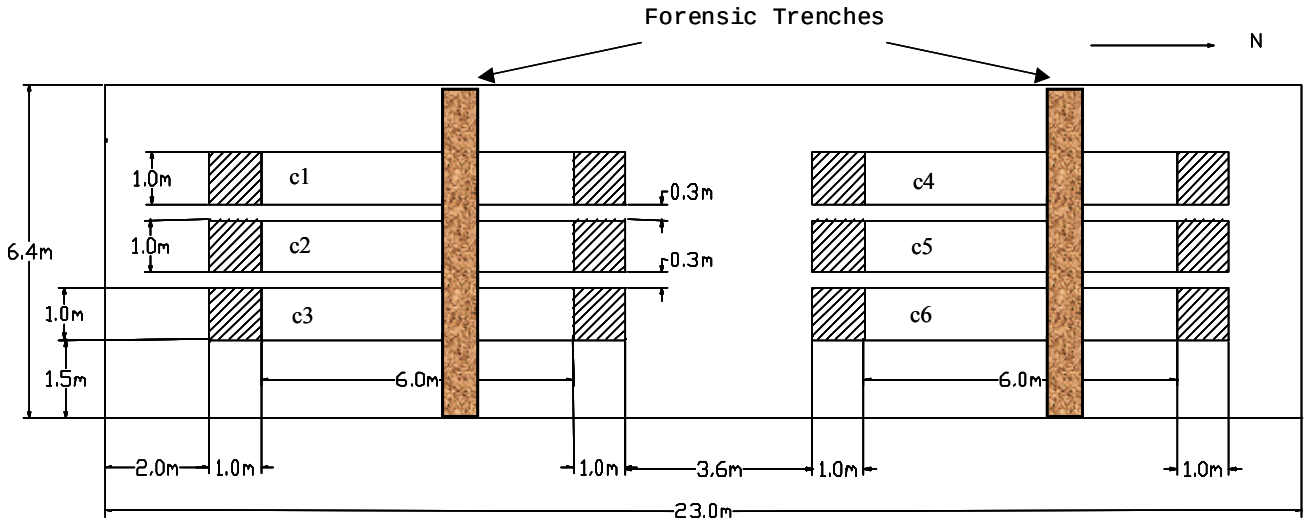

Figure 37. Location of the forensic trenches in Test Section 705.

Figure 38. Forensic trenches across Test Windows 1, 2, and 3.

As soon as the asphalt layer was removed from the trenches, base course samples were collected at 0.20-m (8 in) spacing along one side of the trenches. These samples were used to determine moisture content by the oven-dry method.

Sand cone measurements were conducted at each base and subgrade layer in the trenches. One test location represented the center of the tire path for each test window. In addition, sand cone measurements were conducted outside the test windows.

Figure 39a. Sand cone density measurements in the base course.

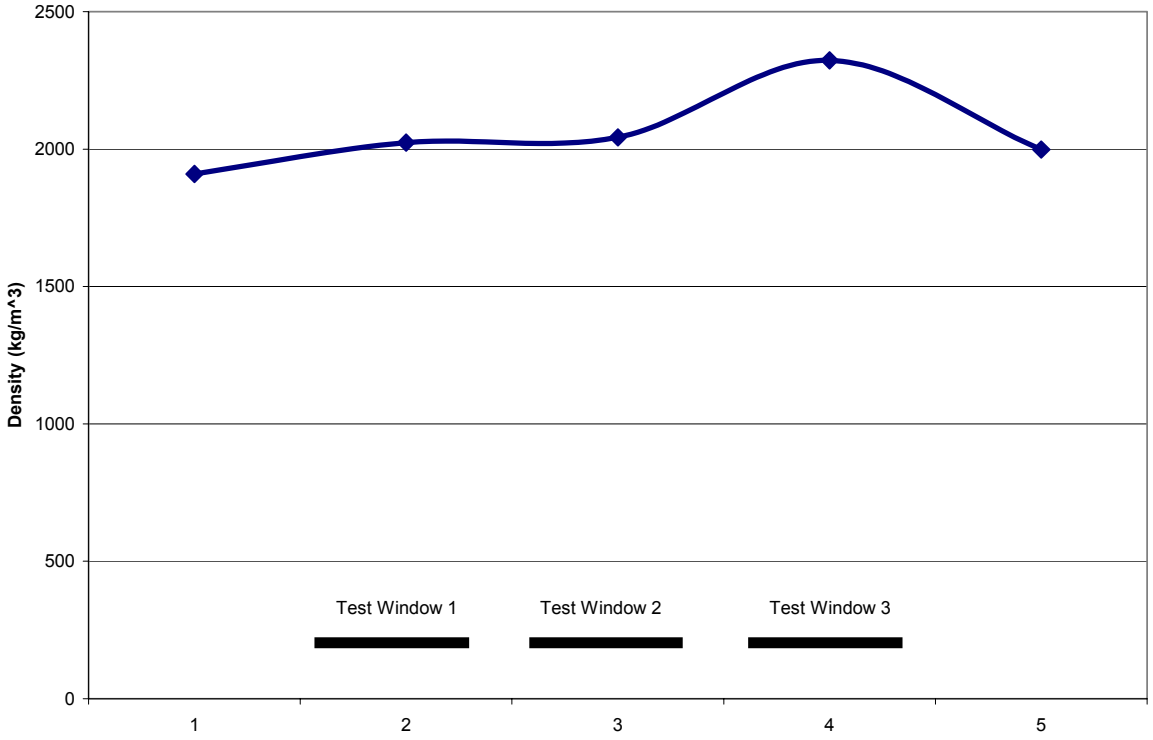

Figure 39b. Base course density measured by the sand cone method in the south trench.

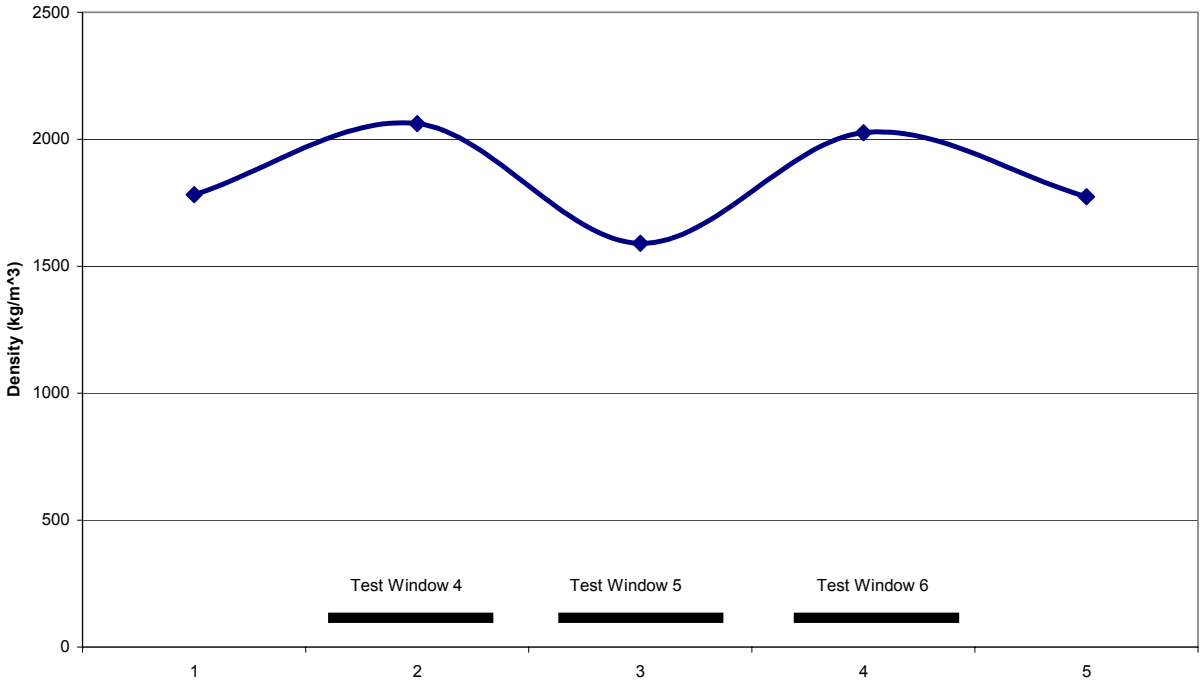

Figure 39c. Base course density measured by the sand cone method in the north trench.

Vane shear tests were conducted at various depths in the subgrade at 33 locations along each trench.

Figure 40a. Vane shear measurements in the subgrade at various depths.

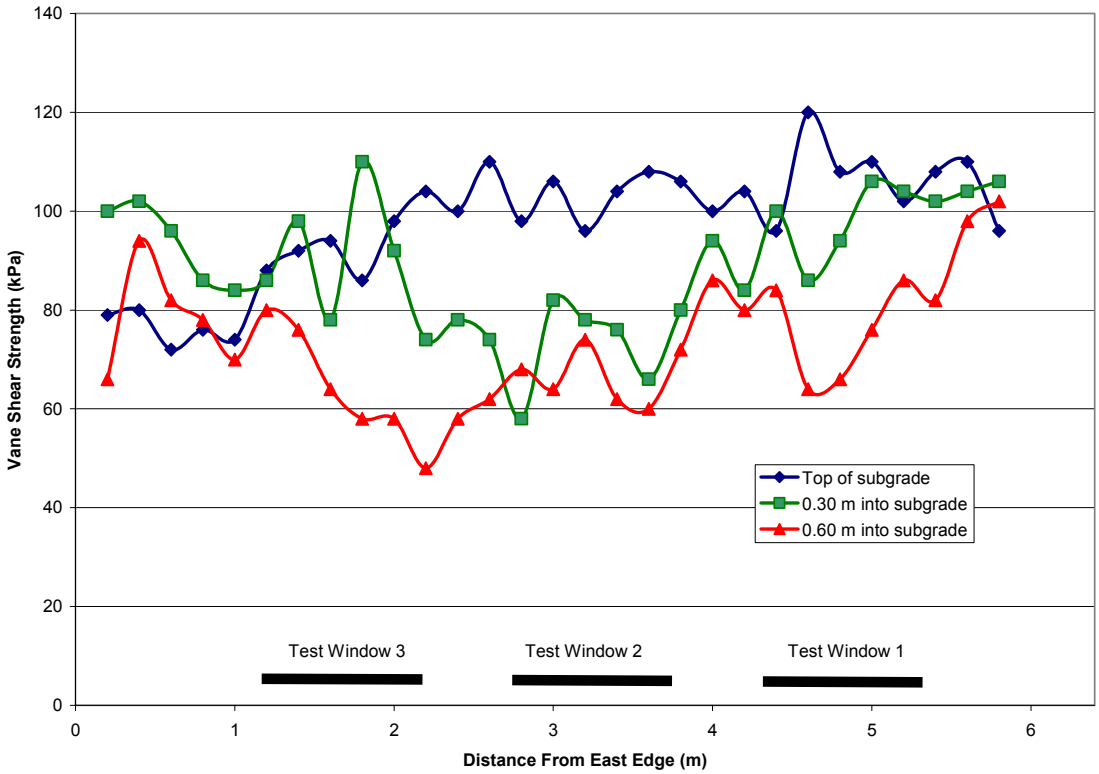

Figure 40b. Vane shear strength measurements in the south trench across Test Windows 1, 2, and 3.

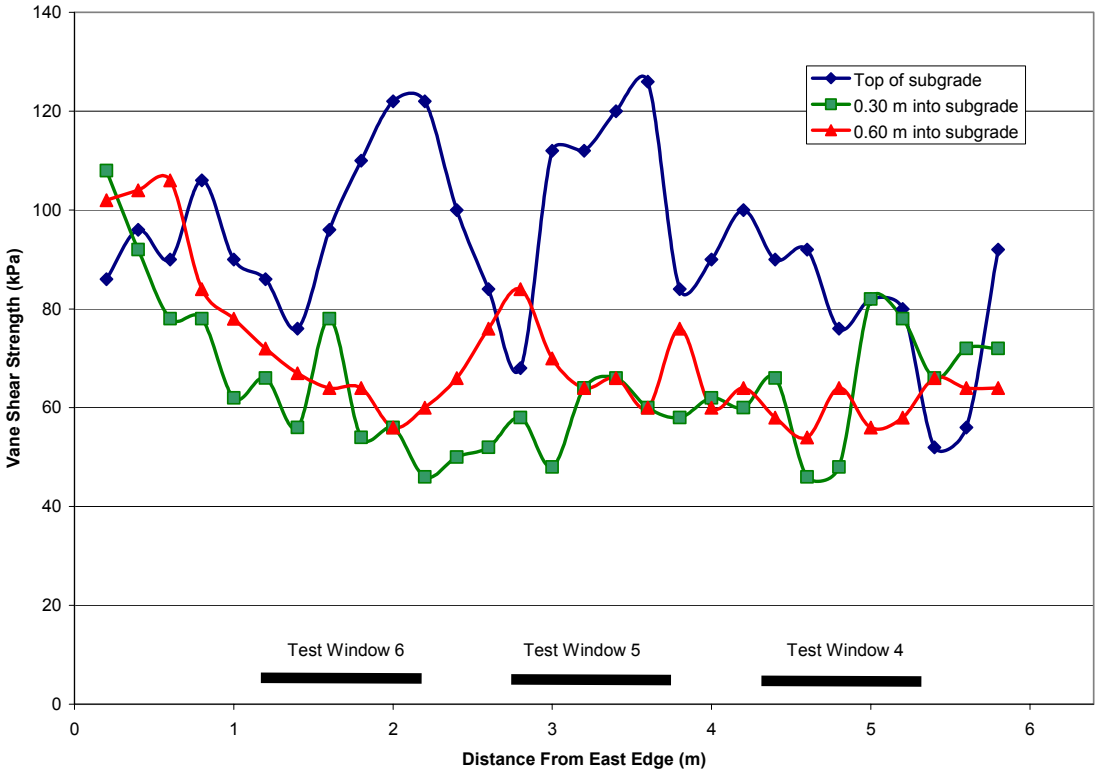

Figure 40c. Vane shear strength measurements in the south trench across Test Windows 4, 5, and 6.

Nuclear moisture and density measurements were taken in the trenches at each layer. The measurements were conducted in the direct mode, i.e., the probe was inserted 0.15 m into the soil. The measurement represents the region of soil between the inseted nuclear source and the receiver in the box of the apparatus. Drive cylinder tests samples were taken in the same volume where the nuclear gauge measurements were taken.

Figure 41a. Nuclear gauge density measurements in the trenches.

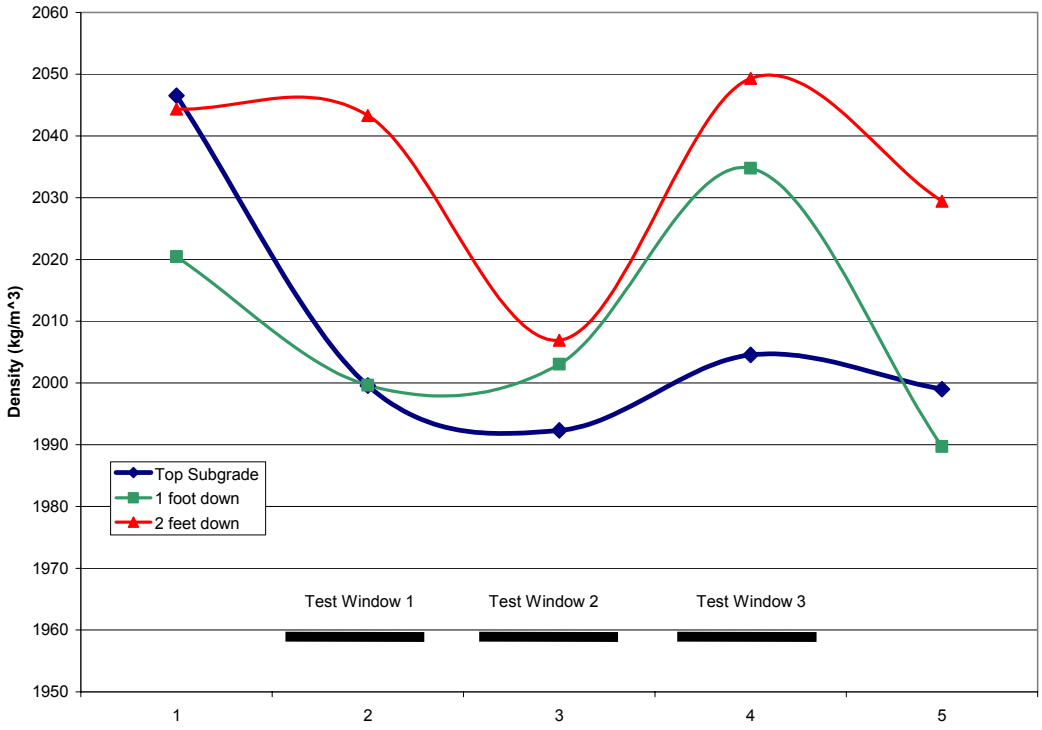

Figure 41b. Soil density at the top of the subgrade in Test Windows 1, 2, and 3, and at the sides of the test windows.

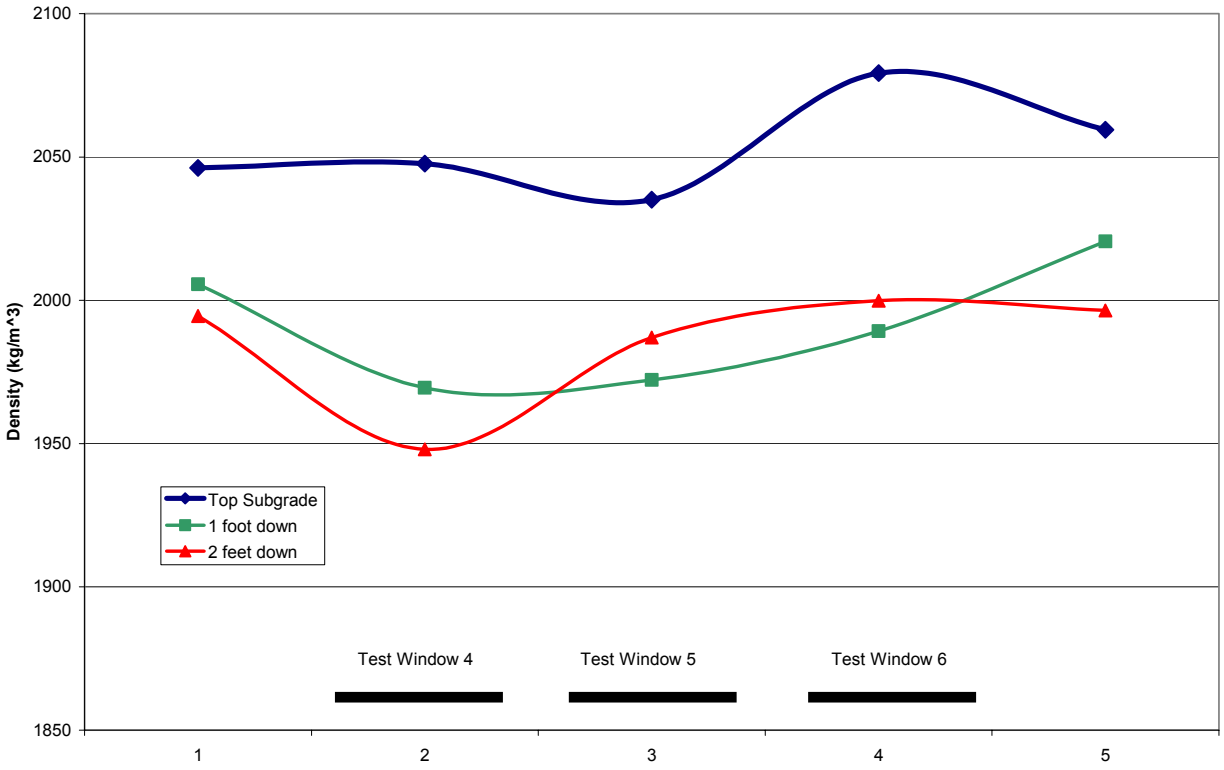

Figure 41c. Soil density at the top of the subgrade in Test Windows 4, 5, and 6, and at the sides of the test windows.

A portable falling weight deflectometer was used to measure the composite soil modulus at various layers in the subgrade at the trenches.

Figure 42a. Portable falling-weight deflectometer measurements in the trenches.

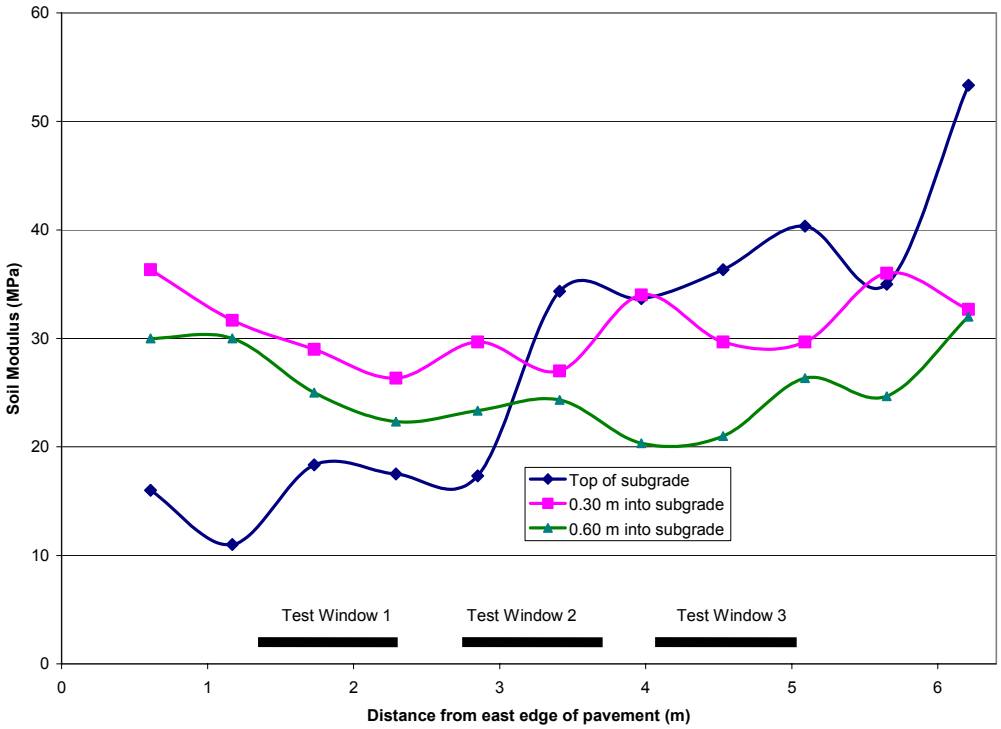

Figure 42b. Soil composite modulus measured with the portable falling-weight deflectometer in the south trench.

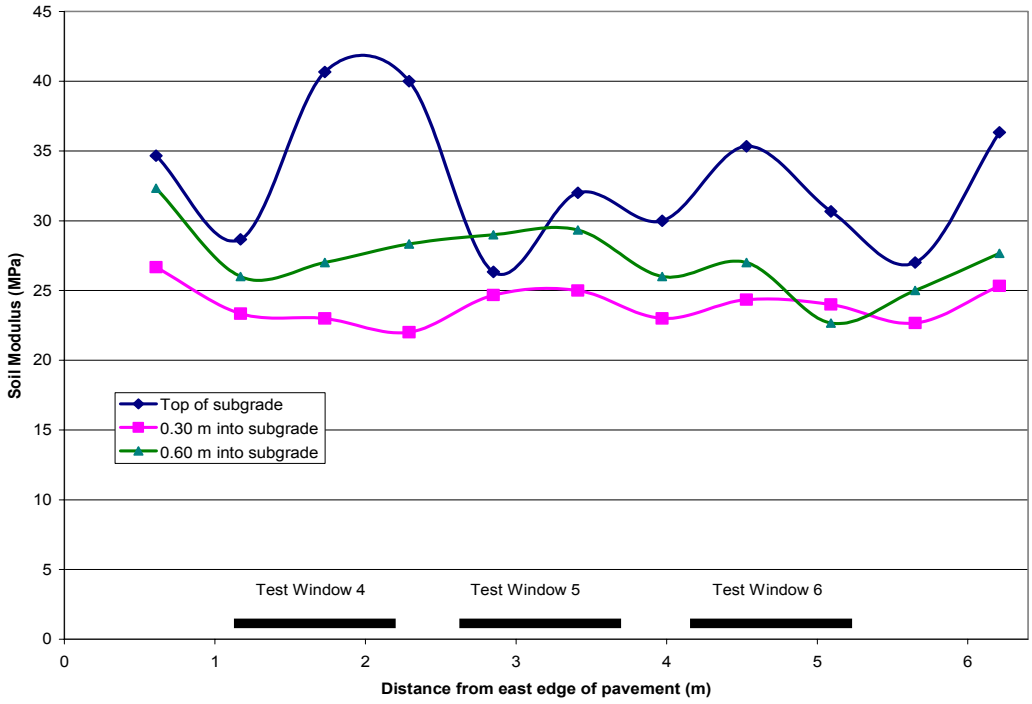

Figure 42c. Soil modulus as measured with the portable falling-weight deflectometer in the north trench.

Dynamic Cone Penetrometer (DCP) measurements were conducted in the trenches at each test window in the traffic area and at each side of the trenches outside the traffic area. DCP tests were initiated on the top of the subgrade, at 0.30 m and at 0.60m depths into the subgrade. The DCP measurements were correlated to California Bearing Ratio (CBR) values.

The DCP readings were correlated to California bearing ratio (CBR) values by the equation:

$$\text{Log CBR} = 2.46 - 1.12 \times \log \text{DCP} \qquad \text{Equation 4}$$

where DCP is in mm/blow

This correlation was developed at the US Army Corps of Engineers Waterways Experiment Station (WES) (Webster at al. 1992). WES developed the above correlation based on testing of a variety of soils. The DCP test apparatus used at CRREL was manufactured by Kessler Soils Engineering Products, Inc. (http://www.kesslerdcp.com/info.html). The DCP–CBR conversions were obtained using an automated Excel spreadsheet provided by the instrument manufacturer. The spreadsheet implements the CBR–DCP correlations developed by WES.

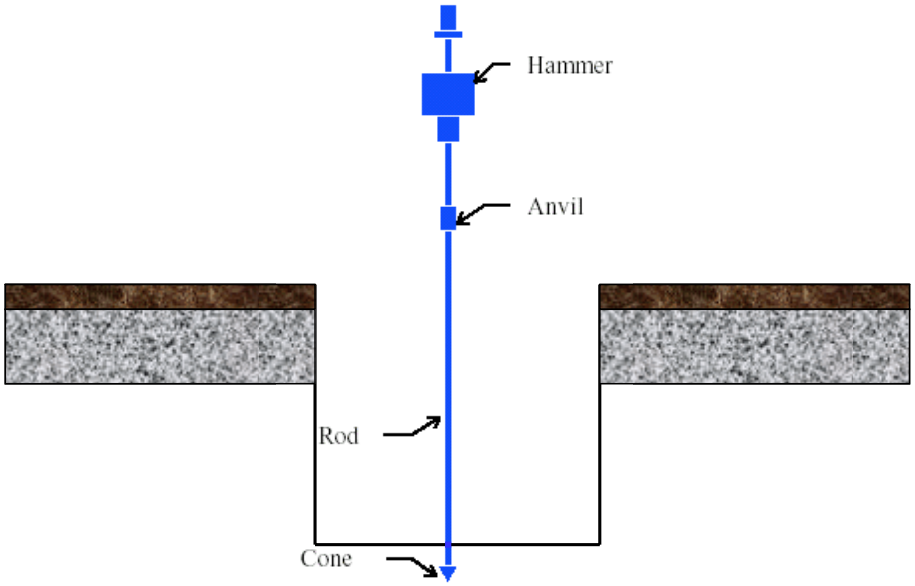

Figure 43a. Dynamic cone penetrometer measurements in the trenches.

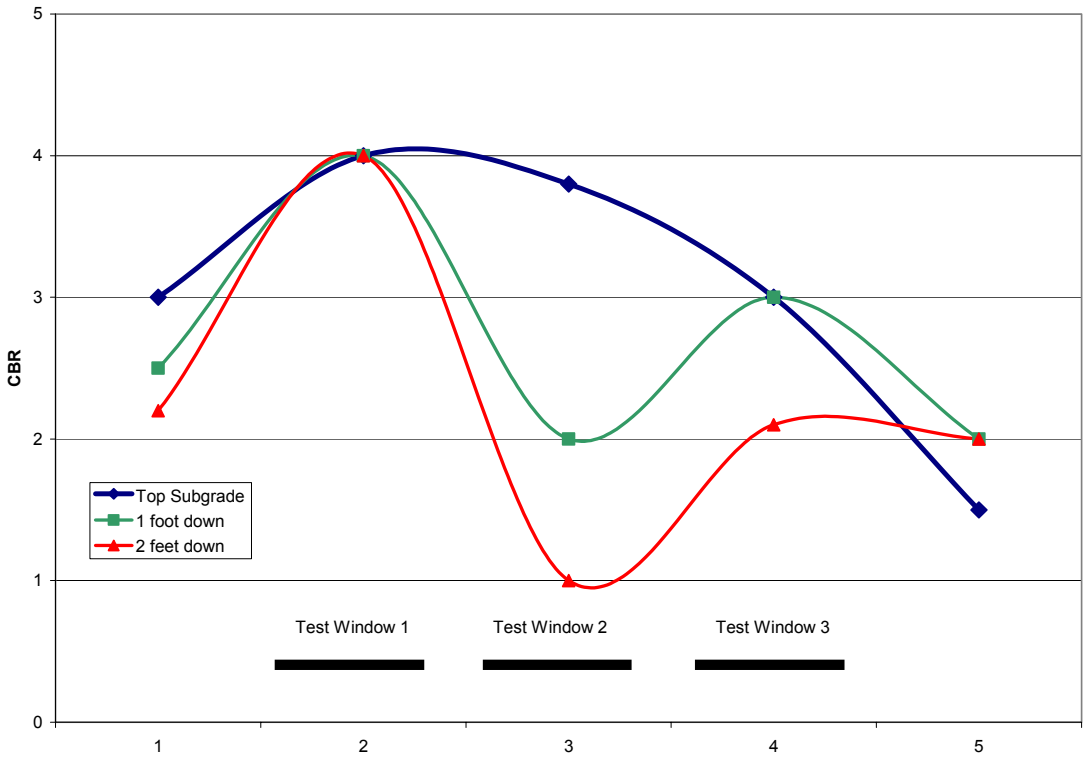

Figure 43b. CBR values obtained from DCP measurements in the south trench.

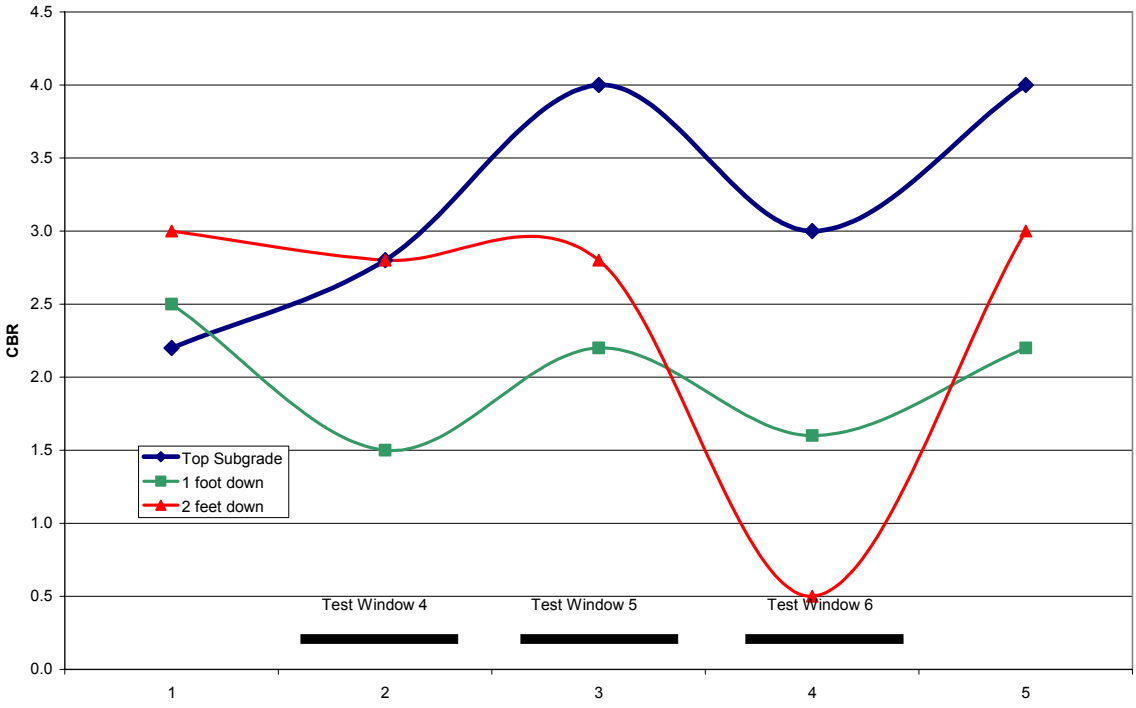

Figure 43c. CBR values obtained from DCP measurements in the north trench.

When the trenches were completed,one wall of the trench was carefully cleaned to be able to measure the actual thickness of the asphalt concrete and the base course at the end of the traffic tests.

Table 18. Thickness of asphalt and base course layers at the center of each test window.

	Thickness (mm)			
Test Window	Under Wheel Path AC	Base Course	Outside of Test Window AC	Base Course
1	88.9	241.3	129.5	241.3
2	146.1	209.6	129.5	241.3
3	81.4	237.1	131.2	254.0
4	70	233	119	250
5	188	191	119	262
6	80	230	110	232

The cross section of the trenches revealed details of irregularities in asphalt concrete thickness and of deformations caused by traffic loads.

Figure 44. Cross section of the asphalt concrete showing asphalt material filling ruts created by construction traffic.

Oven dry moisture tests were conducted on samples taken from the base. The oven dry moisture test results are presented in Figures 117 through 119.

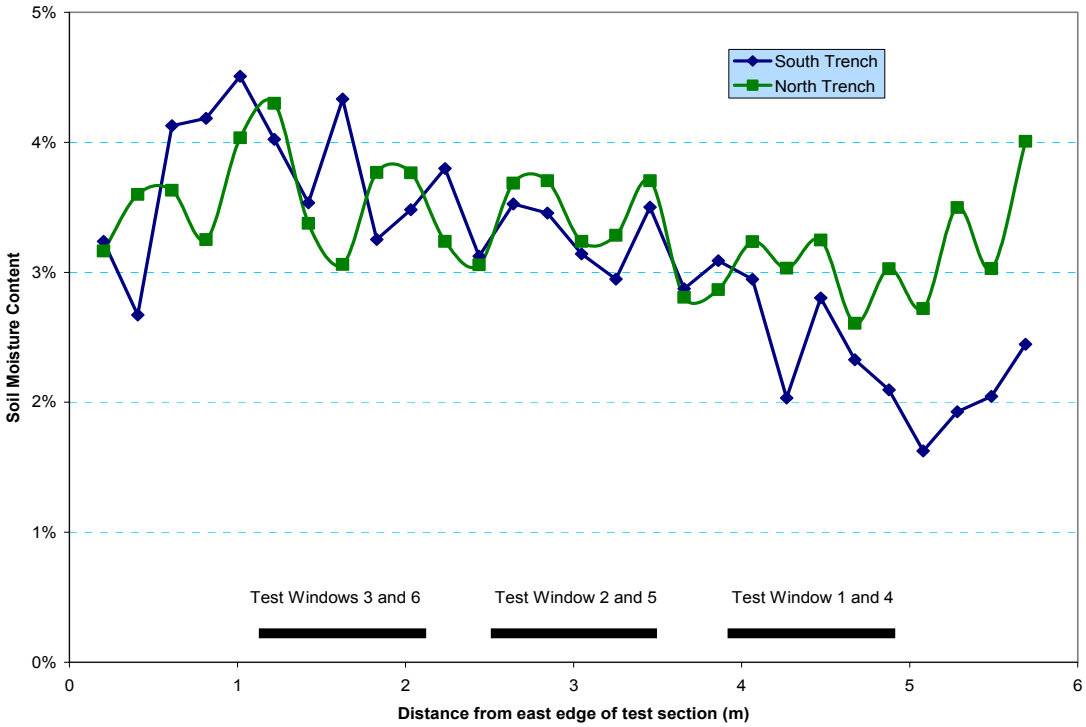

Figure 45. Gravimetric moisture content in the base course.

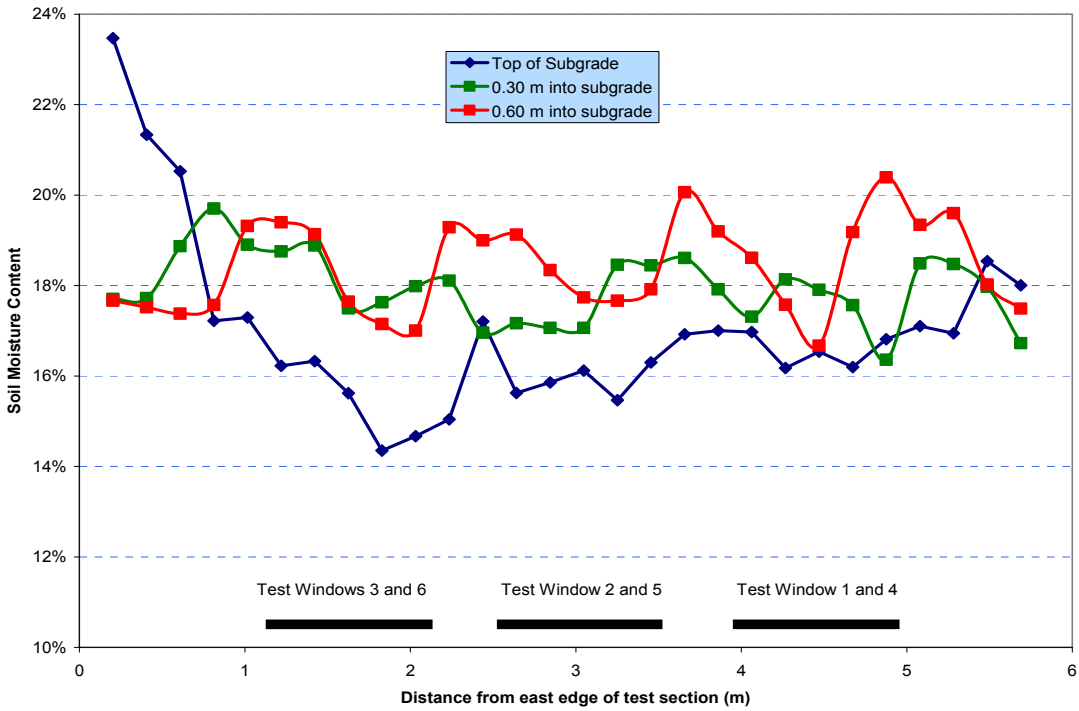

Figure 46a. Gravimetric moisture content in subgrade in the south trench.

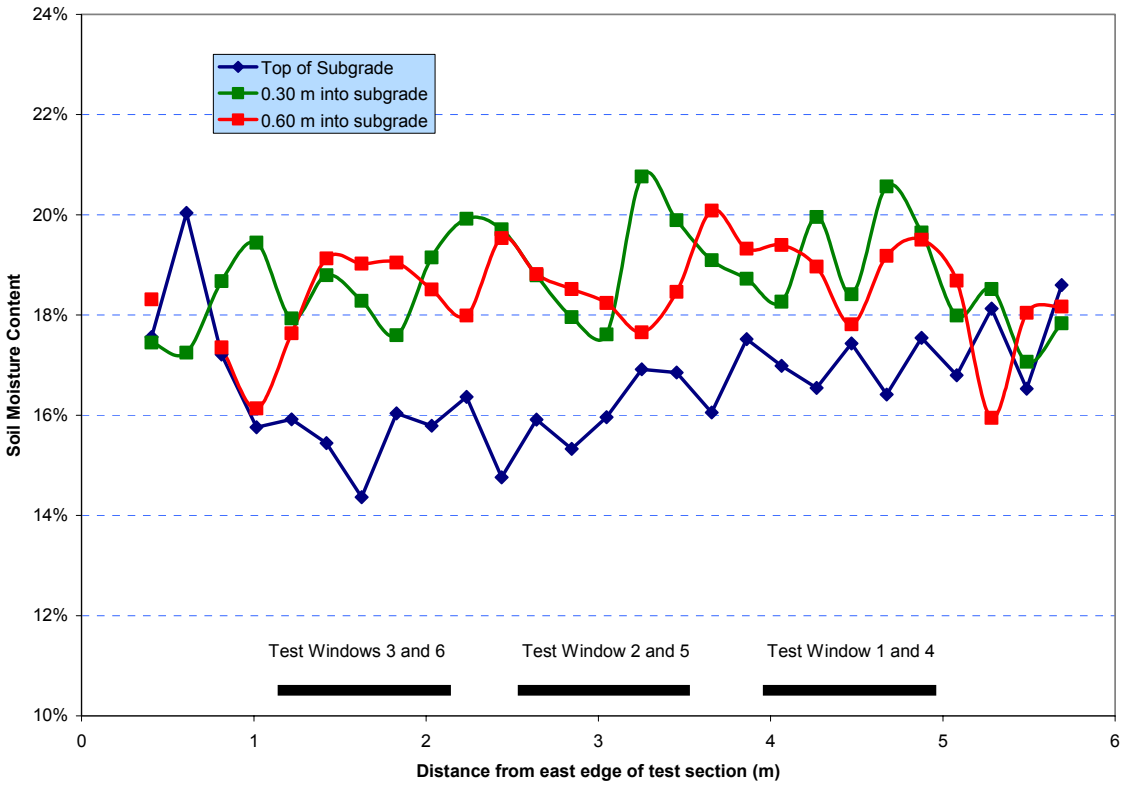

Figure 46b. Gravimetric moisture content in subgrade in the north trench.

Forensic Observations

Rutting, asphalt concrete cracking and base course deformations were abundant in test section 705. During HVS traffic testing, dramatic pavement surface deflections were observed. The deformations were in part resilient and in a part permanent.

When the base course was removed in the trenches, water was observed ponded at the bottom of the base course and on top of the subgrade soil. It appears that moisture was squeezed out of the subgrade. The subgrade soil was extremely soft and muddy at the top of the subgrade, but less muddy and less soft only a few milimeters into the subgrade. If moisture was squeezed from the subgrade by the application of traffic loads, this may explain the rapid rutting observed. This suggests that the subgrade soil has undergone significant consolidation. The DCP correlated CBR values obtained in the subgrade during the forensic evaluation are larger than those obtained for the A-4 soil at 23 percent gravimetric water content during construction. The subgrade soil samples from the trenches had lower moisture content than the moisture content of the subgrade soil during the construction.

Because of the soft subgrade soil, the ruts from one test window extended into the area of the neiboring test windows. For experiments with soft soils, the lateral space between test windows may need to be extended to avoid superposition of effects across test windows. In this test section, Test Window 6 was severely damage by a combination of the extension of the rut in the neighboring test window 5 and the pressures applied by the HVS supports while testing other test windows.

The thickness of the asphalt concrete (AC) varied from 25 mm to 178 mm, but the thickness at most locations was approximately 80 mm. The extreme thickness variations occurred where the trucks travelled to load the paver during construction. The ruts left by the trucks were filled with AC. There were only two small areas where the thickness was less than the intended 76 mm. It is possible that base course material displaced from nearby truck ruts may have cummulated at these locations.

9 SUMMARY AND CONCLUSIONS

The current test section, code named 705, is one of three test sections built with subgrade soil AASHTO type A-4. The first A-4 test section was built at optimum moisture content of 17 percent. The second A-4 test section was built at 19 percent moisture content. Test section 705 was built with A-4 soil at 23 percent moisture content. A correlation of laboratory CBR and moisture content for this soil (Figure 47) shows that this soil becomes unstable (CBR<1) near 23 percent moisture content. Small amounts of moisture concentration due to mechanical action or thermodynamic effects may increase the soil moisture content enough to reach the unstable range. The forensic evaluation suggested that significant soil consolidation occurred as evidenced by water ponding on top of the subgrade, reduction of moisture content in most of the subgrade as compared to the construction conditions, and large surface ruts.

The subgrade soil was made predominantly of fine soil particles. Approximately 85 percent of the A-4 soil particles passed the 0.074-mm (#200) sieve. At 23 percent moisture content, this soil may exhibit significant time-dependent viscous behavior. It was observed that the supports of the HVS were creeping in the pavement despite extra wood planks and boards that helped spread the load.

The finished subgrade was unable to withstand normal construction traffic. The paving equipment left large ruts that became filled with asphalt concrete causing large variations in asphalt concrete thickness. Even at relatively low traffic load, the pavement test section develop ruts beyond failure with only small number of load applications.

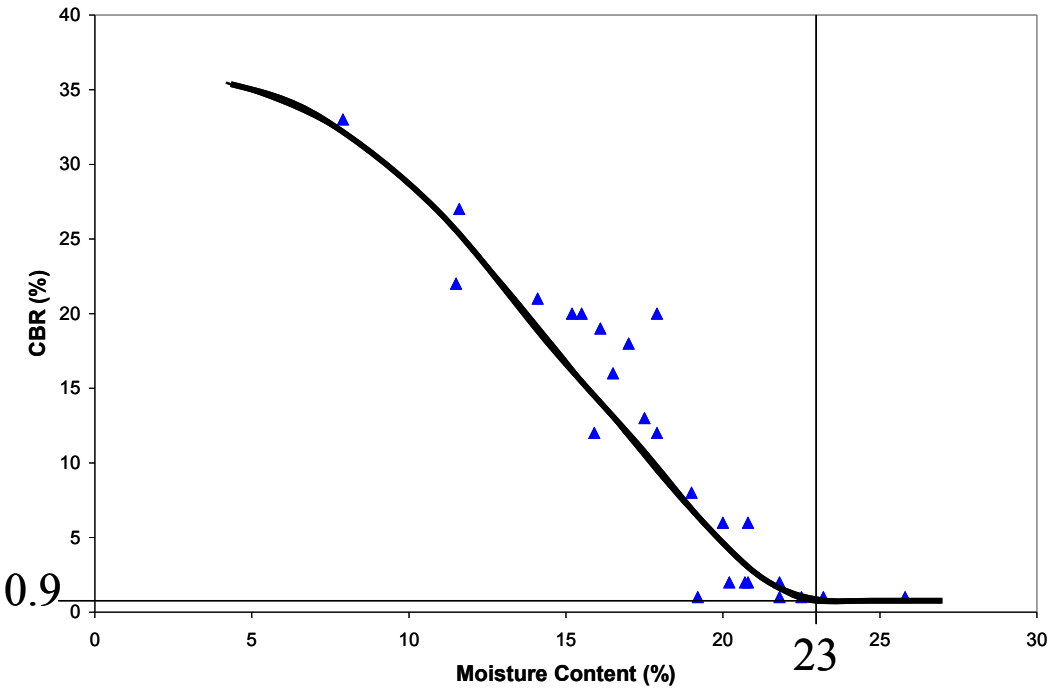

Figure 47. Moisture-CBR relationship for the A-4 subgrade soil

Figure 48. Ruts observed on top of the base course during the paving operation.

Two test windows were tested at three pass levels, two test windows were tested for only two pass levels, one test window lasted only 50 passes, and another test window was too damaged by the extension of traffic damage from a neighboring test window.

The stress cells registered unusually small values perhaps because of lack of support from its substrate. This fact coupled with having data for only 1, 2 or 3 pass levels inhibited the traditional analysis of the stress data. Dramatic dynamic and permanent deformations developed upon application of traffic loads. Much can be learned from the behavior of a weak pavement, but, in order to develop predictions of pavement performance, more stress-strain measurements are needed. Two points in a non-linear graph cannot properly describe stress or strain development.

During the forensic examination, it was found that the subgrade moisture content was lower than the moisture content measured during the subgrade construction. However, at the bottom of the base course, there was abundance of bulk water standing on top of the subgrade. This finding suggests that some consolidation of the subgrade soil may have occurred.

In three out of the five longitudinal rut profiles shown in Figures 31, 32 and 33, there appears to be a trend whereby deeper ruts occurred at the end of the test window where the tire first applies the load prior to running along the test window. This suggests that, for this subgrade soil at high moisturecontent, the permanent deformation is larger where the load is applied slowly, and some resistance to deformation occurs when the load travels along the tire path. This suggests significant visco-plastic behaivor of the subgrade soil. It is therefore understandable that the FWD backcalculations were dificult to obtain without altering the thickness of some layers beyond the measured values. The backcalculation procedure assumes linear elastic behavior of the pavement materials. One HVS load cycle was applied every 6 seconds. With a subgrade soil at or near saturation, this rate of traffic may produce cummulative pumping from one end of the test window to the other. This hypothesis may be tested in future experiments by including forensic exploration at both ends of the test window. The current forensic exploration included only one transversal trench.

REFERENCE

Janoo, V., L. Irwin, R. Eaton, and R. Haehnel, (2002) “Pavement Subgrade Performance Study: Project Overview, ERDC Report TR15.

Lide, David R., (1994) Handbook of Chemistry and Physics, 74th edition, CRC press.

Webster, S.L., R.H. Grau, and T.P. Williams (1992) Description and application of dual mass dynamic cone penetrometer. USACE Waterways Experimental Station, Vicksburg, Mississippi, Instruction Report GL-92-3.

APPENDIX A: FROST EFFECTS RESEARCH FACILITY (FERF)

DESCRIPTION OF FROST EFFECTS RESEARCH FACILITY

The FERF is a 2,700 m^2 environmentally controlled building. The overall facility is 56 m long by 31 m wide (Figure A-1).

Figure A-1. Frost Effects Research Facility (FERF)

Within the facility are 12 test cells, which are 6.4 m wide. Eight of the cells (TC-1 to TC-8) are 7.6 m long and 2.4 m deep. The remaining 4 cells (TB-9 to TB-12) are of the same width but are 11.3 m long and 3.7 m deep, A- 2. They can be used individually for smaller experiments or combined in a variety of ways to accommodate larger projects. In addition, the cells can be made impermeable to simulate the raising and lowering of the water table.

The ambient air temperature within the facility can be controlled from -4 °C to 24 °C with a ± 2 °C tolerance. The temperatures in the test cell can be further reduced or increased using surface panels (- 32 °C to 49 °C).

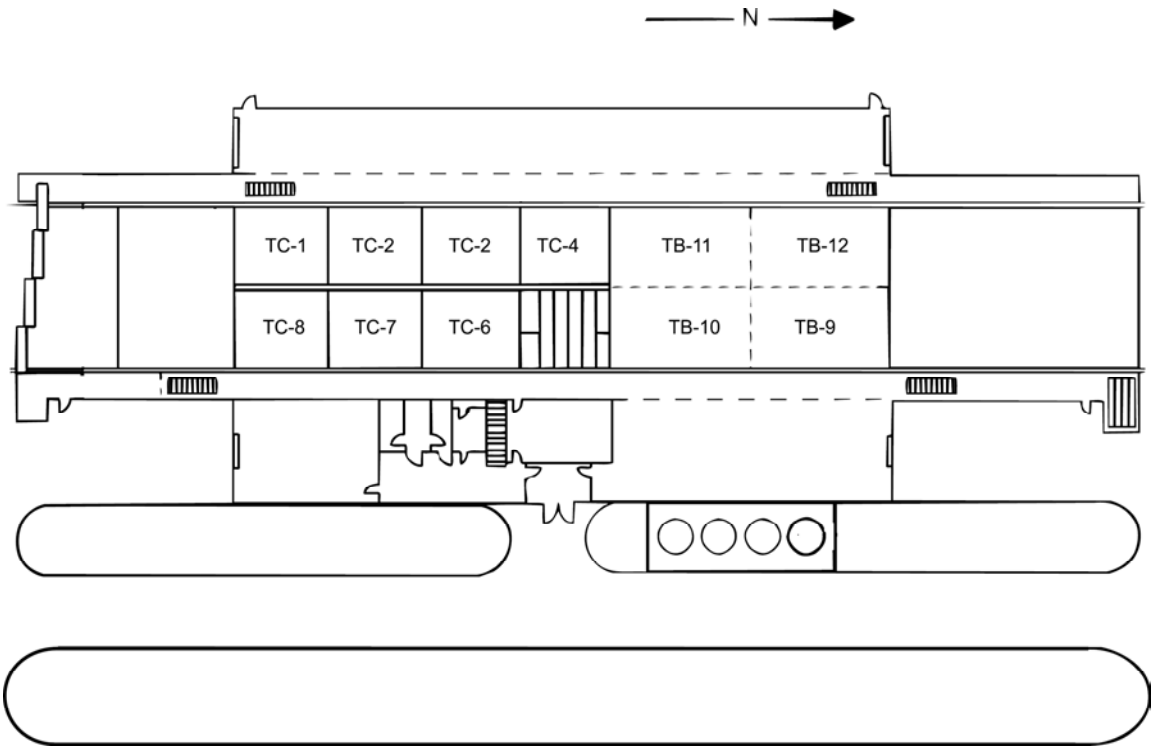

Figure A-2. Plan view of test basins in the Frost Effects Research Facility (FERF)

APPENDIX B: CONSTRUCTION DATA

Table B-1. As constructed density and gravimetric moisture content in the base course by nuclear gauge method.

Location	Dry Density		Moisture
Number*	(Lb/cu.ft)	(kg/cu.m)	(%)
1	118.4	1897	3.1
2	126.4	2025	2.9
3	120.1	1924	3.6
4	119.9	1921	3.8
5	124.3	1991	3.4
6	127.4	2041	2.8
7	124.7	1998	3.5
8	126.5	2027	3.2
9	121.4	1945	3.7
10	119.2	1910	3.6
11	120.8	1935	3.0
12	127.3	2039	3.7
13	127.9	2049	3.5
14	124.2	1990	3.4
15	121.4	1945	2.8
16	127.1	2036	3.4
17	120.9	1937	3.9
18	126.5	2027	3.6
19	119.8	1919	2.9
20	120.6	1932	3.5
21	127.2	2038	3.0
22	125.4	2009	3.4
23	120.1	1924	3.6
24	108.4	1737	3.0
25	126.5	2027	2.9
26	124.6	1996	3.2
27	127.3	2039	3.1
28	123.5	1978	3.5
29	123.6	1980	3.2
30	124.0	1986	3.8

* Test locations are mapped with respect to the test windows in Figure 12.

Table B-2. As constructed density and gravimetric moisture content near the top of the subgrade by nuclear gauge method.

Location	Dry Density		Moisture
Number*	(Lb/cu.ft)	(kg/cu.m)	(%)
1	102.1	1897	23.1
2	103.0	2025	22.1
3	104.1	1924	21.9
4	101.8	1921	22.6
5	101.2	1991	23.2
6	101.9	2041	22.5
7	100.2	1998	24.7
8	103.6	2027	22.6
9	102.1	1945	23.0
10	102.8	1910	22.8
11	103.1	1935	22.2
12	101.4	2039	23.2
13	103.1	2049	22.7
14	101.0	1990	22.9
15	100.5	1945	23.7
16	103.8	2036	22.8
17	100.4	1937	23.4
18	102.6	2027	22.5
19	104.5	1919	21.4
20	103.4	1932	22.4
21	105.2	2038	21.0
22	104.1	2009	21.6
23	102.1	1924	23.0
24	101.4	1737	23.5
25	101.8	2027	23.1
26	102.4	1996	22.8
27	101.5	2039	23.2
28	103.1	1978	22.8
29	105.9	1980	20.9
30	105.0	1986	21.4

* Test locations are mapped with respect to the test windows in Figure 12.

Table B-3. As constructed density and gravimetric moisture content at depth 0.38 m from the top of the subgrade by nuclear gauge method.

Location	Dry Density		Moisture
Number*	(Lb/cu.ft)	(kg/cu.m)	(%)
1	102.9	1648.3	23.7
2	106.5	1706.0	23.1
3	104.3	1670.7	22.6
4	103.9	1664.3	23.4
5	104.7	1677.1	22.2
6	102.6	1643.5	21.4
7	104.5	1673.9	22.7
8	103.0	1649.9	23.2
9	103.9	1664.3	22.8
10	104.2	1669.1	22.9
11	102.9	1648.3	23.7
12	104.8	1678.7	22.1
13	102.4	1640.3	23.7
14	104.6	1675.5	22.4
15	101.8	1630.7	24.0
16	104.2	1669.1	21.4
17	103.2	1653.1	22.8
18	102.3	1638.7	23.5
19	102.9	1648.3	23.2
20	105.6	1691.6	20.9
21	104.0	1665.9	22.4
22	102.9	1648.3	23.5
23	101.9	1632.3	23.9
24	102.3	1638.7	22.8
25	102.9	1648.3	23.2
26	105.0	1681.9	21.8
27	104.1	1667.5	22.9
28	101.8	1630.7	23.8
29	102.4	1640.3	23.4
30	101.8	1630.7	23.2

* Test locations are mapped with respect to the test windows in Figure 12.

Table B-4. As constructed density and gravimetric moisture content at depth 0.69 m from the top of the subgrade by nuclear gauge method.

Location	Dry Density		Moisture
Number*	(Lb/cu.ft)	(kg/cu.m)	(%)
1	103.1	1651.5	23.1
2	104.0	1665.9	22.9
3	104.2	1669.1	22.6
4	105.0	1681.9	22.4
5	102.1	1635.5	23.6
6	105.9	1696.4	21.6
7	104.3	1670.7	24.0
8	104.6	1675.5	24.2
9	102.8	1646.7	23.6
10	102.0	1633.9	23.2
11	102.6	1643.5	22.4
12	106.0	1698.0	20.9
13	103.8	1662.7	23.2
14	103.9	1664.3	23.0
15	101.0	1617.9	24.1
16	103.8	1662.7	23.6
17	103.1	1651.5	23.0
18	103.6	1659.5	22.8
19	103.8	1662.7	22.9
20	104.6	1675.5	21.6
21	104.0	1665.9	22.8
22	103.1	1651.5	23.1
23	103.2	1653.1	23.0
24	100.9	1616.3	24.6
25	103.6	1659.5	21.4
26	103.4	1656.3	22.8
27	101.8	1630.7	23.6
28	101.5	1625.9	23.2
29	101.8	1630.7	22.6
30	102.8	1646.7	22.9

* Test locations are mapped with respect to the test windows in Figure 12.

Table B-5. As constructed density and gravimetric moisture content at depth 0.99 m from the top of the subgrade by nuclear gauge method.

Location	Dry Density		Moisture
Number*	(Lb/cu.ft)	(kg/cu.m)	(%)
1	102.1	1635.5	23.1
2	103.0	1649.9	22.1
3	104.1	1667.5	21.9
4	101.8	1630.7	22.6
5	101.2	1621.1	23.2
6	101.9	1632.3	22.5
7	100.2	1605.1	24.7
8	103.6	1659.5	22.6
9	102.1	1635.5	23.0
10	102.8	1646.7	22.8
11	103.1	1651.5	22.2
12	101.4	1624.3	23.2
13	103.1	1651.5	22.7
14	101.0	1617.9	22.9
15	100.5	1609.9	23.7
16	103.8	1662.7	22.8
17	100.4	1608.3	23.4
18	102.6	1643.5	22.5
19	104.5	1673.9	21.4
20	103.4	1656.3	22.4
21	105.2	1685.1	21.0
22	104.1	1667.5	21.6
23	102.1	1635.5	23.0
24	101.4	1624.3	23.5
25	101.8	1630.7	23.1
26	102.4	1640.3	22.8
27	101.5	1625.9	23.2
28	103.1	1651.5	22.8
29	105.9	1696.4	20.9
30	105.0	1681.9	21.4

* Test locations are mapped with respect to the test windows in Figure 12.

Table B-6. As constructed Vane shear in the subgrade.

Test Location Number*	Vane Shear (kPa)			
	Depth from top of subgrade (m)			
	0.08	0.38	0.69	0.99
1	34	26	26	48
2	46	38	30	56
3	42	18	28	38
4	46	40	26	30
5	46	28	29	32
6	52	32	36	36
7	50	34	32	38
8	46	42	34	40
9	42	30	36	34
10	46	26	28	36
11	60	32	38	48
12	54	26	30	54
13	32	30	30	44
14	36	34	31	42
15	34	28	26	44
16	28	36	36	46
17	28	30	44	46
18	30	32	36	36
19	28	28	28	48
20	32	34	28	22
21	28	36	24	38
22	30	26	27	42
23	44	44	46	44
24	52	36	40	46
25	58	48	24	31
26	42	54	26	44
27	38	58	43	58
28	48	56	48	54
29	36	52	53	52
30	28	38	33	38
31	32	26	26	42
32	24	24	34	26
33	38	32	26	34
34	22	38	24	40
35	36	38	32	44
36	38	32	26	35

* Test locations are mapped with respect to the test windows in Figure 17.

Table B-7. Nuclear gauge asphalt concrete density and air voids

Location Number*	Density (Lb/cu.ft)	Density (kg/cu.m)	Air Voids (%)
1	141.2	2261.8	2.2
2	142.3	2279.4	1.7
3	143.5	2298.7	1.1
4	137.2	2197.7	5.0
5	138.9	2225.0	4.2
6	144.5	2314.7	1.9
7	142.2	2277.8	1.5
8	140.6	2252.2	3.0
9	147.5	2362.7	1.8
10	145.4	2329.1	0.3
11	143.5	2298.7	1.0
12	149.8	2399.6	3.3
13	142.3	2279.4	1.6
14	150.1	2404.4	2.0
15	136.1	2180.1	6.0
16	149.6	2396.4	3.2
17	138.0	2210.6	4.9
18	147.4	2361.1	1.6
19	141.4	2265.0	2.5
20	141.7	2269.8	2.3
21	140.1	2244.2	3.1
22	148.9	2385.2	0.8
23	130.8	2095.2	4.9
24	136.5	2186.5	4.4
25	141.2	2261.8	2.4
26	149.2	2390.0	2.8
27	142.4	2281.0	1.7
28	141.2	2261.8	2.6
29	138.6	2220.2	4.8
30	145.4	2329.1	0.4
31	144.0	2306.7	0.7
32	142.9	2289.0	1.5
33	141.4	2265.0	2.5
34	139.6	2236.2	3.7
35	138.6	2220.2	4.2
36	138.3	2215.4	5.0
37	140.6	2252.2	3.0
38	139.2	2229.8	4.0
39	132.3	2119.2	3.3
40	140.9	2257.0	3.1
41	129.2	2069.6	10.9
42	127.8	2047.2	11.5
43	132.9	2128.9	9.8
44	136.5	2186.5	8.8
45	139.4	2233.0	5.0
46	143.1	2292.2	1.6
47	129.3	2071.2	10.8
48	139.5	2234.6	3.8

APPENDIX C RESULTS OF ASPHALT MIXTURE TESTING

Dr. Vincent C. Janoo
USA CRREL
72 Lyme Road
Hanover, NH 03755-1290

Dr. Janoo,

On November 8, 2001 hot mix asphalt samples were received at the Nebraska Department of Roads Materials and Research Testing Laboratories from the paving performed October 25, 2001 on the CRREL Pavement Subgrade Performance Study, SPR-2(208) test section 705. The mix was submitted in 3 boxes and was produced by Blaktop Inc. of West Lebanon, New Hampshire. The mix was identified as a New Hampshire State DOT Type "C" mix. The following is information supplied by the contractor:

Binder: PG 64-22 from Hudson Liquid Asphalt Corporation – Providence, Rhode Island

Material	**% in Mix**	**Specific Gravity**
Screened Natural Sand	34.0	2.647
Washed Stone Screenings	14.6	2.766
3/8" Crushed Stone	32.9	2.802
½" Crushed Stone	18.5	2.808

Asphalt Content 6.1%

The objective was to report the quality of the mix produced by performing a volumetric analysis, measuring the consensus properties, and testing its performance in the Asphalt Pavement Analyzer. The analysis was somewhat limited due to the fact that all of the materials tested were from the plant produced hot-mix and there were no samples of virgin aggregate taken. Therefore all of the consensus properties were from ignition oven material that is generally affected by the high heat of the burn off process. The following 3 pages are a summary of the test results:

Sieve Analysis (AASHTO T-30)

Sieve	% Retained	% Passing
1”	0.0	100.0
¾”	0.0	100.0
½”	2.3	97.7
3/8”	11.5	88.5
#4	33.6	66.4
#8	43.8	56.2
#16	53.0	47.0
#30	65.4	34.6
#50	77.9	22.1
#100	87.0	13.0
#200	93.1	6.9

Binder Content By Ignition Oven (AASHTO T-308)

6.28 %

Fine Aggregate Angularity (AASHTO T-304, method “A”)

FAA = 45.7

Course Aggregate Angularity (ASTM D5821)

CAA = 97/97

Sand Equivalent (AASHTO T-176)

Sand Equivalent = 81

Flat and Elongated Particles (ASTM D4791, 5:1 ratio)

Flat and Elongated = 3

Aggregate Specific Gravity (AASHTO T-84 and T-85)

Specific Gravity = 2.721 performed on ignition oven sample

Moisture Sensitivity (AASHTO T-283)

TSR = 85.6%

Marshall Test Results

(50 Blow Compaction)

Air Voids = 2.4 %
VMA = 14.8 %
Stability = 3275 lbs
Flow = 14

(75 Blow Compaction)

Air Voids = 1.5 %
VMA = 13.9 %
Stability = 3360
Flow = 14

Gyratory Test Results

(134 Gyrations)

Air Voids @ Ninitial = 6.5 %
Air Voids @ Ndesign = 1.3 %
Air Voids @ Nmax = 0.9 %
VMA = 13.7 %
VFA = 90.6 %

(152 Gyrations)

Air Voids @ Ninitial = 6.7 %
Air Voids @ Ndesign = 0.9 %
Air Voids @ Nmax = 0.5 %
VMA = 13.4 %
VFA = 93.2 %

Asphalt Pavement Analyzer Results

Chamber Environment = 147° F (64°C) Dry Test
Wheel Load 100 lbs (0.44 kN)
Hose Pressure 100 psi (690 kPa)
8000 Load Cycles

Set 1 Results

6.92% Air Voids
Test was discontinued at 4984 Load Cycles with 11.74 mm of rutting

Set 2 Results

6.74% Air Voids
Test was discontinued at 4984 Load Cycles with 11.11 mm of rutting

Set 3 Results

7.12% Air Voids
Test was discontinued at 4984 Load Cycles with 10.66 mm of rutting

This concludes the series of testing on the submitted hot mix samples.
If you have any questions, please feel free to call at 402-479-4677.

Robert C. Rea, P.E.
Pavement Design Engineer
Nebraska Department of Roads